Gastroenterology 2023;164:1137–1151

Stiffness Restricts the Stemness of the Intestinal Stem Cells and Skews Their Differentiation Toward Goblet Cells

Shijie He,[1,2,3,4,*] **Peng Lei**,[1,2,3,4,*] Wenying Kang,[5] Priscilla Cheung,[4,6] Tao Xu,[4,7] Miyeko Mana,[8] Chan Young Park,[9] Hongyan Wang,[1,4] Shinya Imada,[8] Jacquelyn O. Russell,[4,6] Jianxun Wang,[1,2,3,4] Ruizhi Wang,[10] Ziheng Zhou,[1,2,3,4] Kashish Chetal,[4,11] Eric Stas,[4,12] Vidisha Mohad,[1,4] Peter Bruun-Rasmussen,[13] Ruslan I. Sadreyev,[4,11,14] Richard A. Hodin,[1,4] Yanhang Zhang,[10] David T. Breault,[4,12,15] Fernando D. Camargo,[4,6,15] Ömer H. Yilmaz,[8] Jeffrey J. Fredberg,[9] and Nima Saeidi[1,2,3,4,15]

[1]Division of Gastrointestinal and Oncologic Surgery, Department of Surgery, Massachusetts General Hospital, Boston, Massachusetts; [2]Center for Engineering in Medicine and Surgery, Department of Surgery, Massachusetts General Hospital, Boston, Massachusetts; [3]Shriners Hospital for Children, Boston, Massachusetts; [4]Harvard Medical School, Boston, Massachusetts; [5]Department of Otolaryngology–Head and Neck Surgery, Stanford Medical School, Stanford, California; [6]Stem Cell Program and Department of Hematology/Oncology, Children's Hospital, Boston, Massachusetts: [7]Section on Pathophysiology and Molecular Pharmacology, Joslin Diabetes Center, Boston, Massachusetts; [8]Koch Institute for Integrative Cancer Research, Massachusetts Institute of Technology, Cambridge, Massachusetts; [9]Department of Environmental Health, Harvard T.H. Chan School of Public Health, Boston, Massachusetts; [10]Department of Mechanical Engineering, Boston University, Boston, Massachusetts; [11]Department of Molecular Biology, Massachusetts General Hospital, Boston, Massachusetts; [12]Division of Endocrinology, Boston Children's Hospital, Boston, Massachusetts; [13]Department of Clinical Immunology, Rigshospitalet, Copenhagen University Hospital, Copenhagen, Denmark; [14]Department of Pathology, Massachusetts General Hospital, Boston, Massachusetts; and [15]Harvard Stem Cell Institute, Cambridge, Massachusetts

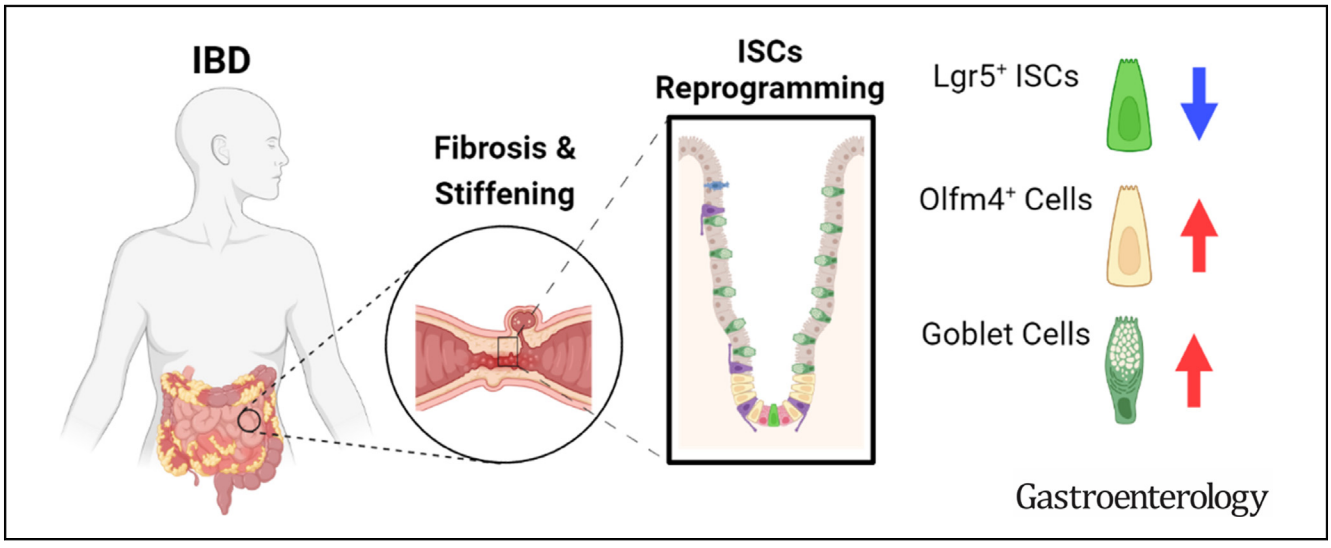

BACKGROUND & AIMS: Fibrosis and tissue stiffening are hallmarks of inflammatory bowel disease (IBD). We have hypothesized that the increased stiffness directly contributes to the dysregulation of the epithelial cell homeostasis in IBD. Here, we aim to determine the impact of tissue stiffening on the fate and function of the intestinal stem cells (ISCs). **METHODS:** We developed a long-term culture system consisting of 2.5-dimensional intestinal organoids grown on a hydrogel matrix with tunable stiffness. Single-cell RNA sequencing provided stiffness-regulated transcriptional signatures of the ISCs and their differentiated progeny. YAP-knockout and YAP-overexpression mice were used to manipulate YAP expression. In addition, we analyzed colon samples from murine colitis models and human IBD samples to assess the impact of stiffness on ISCs in vivo. **RESULTS:** We demonstrated that increasing the stiffness potently reduced the population of LGR5^{+} ISCs and KI-67^{+}–proliferating cells. Conversely, cells expressing the stem cell marker, olfactomedin-4, became dominant in the crypt-like compartments and pervaded the villus-like regions. Concomitantly, stiffening prompted the ISCs to preferentially differentiate toward goblet cells. Mechanistically, stiffening increased the expression of cytosolic YAP, driving the extension of olfactomedin-4^{+} cells into the villus-like regions, while it induced the nuclear translocation of YAP, leading to preferential differentiation of ISCs toward goblet cells. Furthermore, analysis of colon samples from murine colitis

models and patients with IBD demonstrated cellular and molecular remodeling reminiscent of those observed in vitro. **CONCLUSIONS:** Collectively, our findings highlight that matrix stiffness potently regulates the stemness of ISCs and their differentiation trajectory, supporting the hypothesis that fibrosis-induced gut stiffening plays a direct role in epithelial remodeling in IBD.

Keywords: IBD; Fibrosis; Stiffening; Intestinal Organoids; Intestinal Stem Cells.

WHAT YOU NEED TO KNOW

BACKGROUND AND CONTEXT

Fibrosis and tissue stiffening are hallmarks of inflammatory bowel disease (IBD). Yet, it is unclear how the tissue stiffening impacts the fate of intestinal stem cells (ISCs).

NEW FINDINGS

Stiffening reduces the population of $Lgr5^{hi}$ ISCs and $Ki67^{+}$ progenitor cells, extends Olfm4 expression from the crypt-like compartments into the villus-like regions, and promotes ISCs to preferentially differentiate to goblet cells.

LIMITATIONS

Directly preventing or inhibiting intestinal fibrosis and stiffening in mice with colitis is not included due to lack of reliable strategies. The colitis mouse model was performed using male mice.

CLINICAL RESEARCH RELEVANCE

We elucidated how intestinal stiffening reprograms the ISC fate during IBD, leading to intestinal epithelial deterioration. In addition, the Olfm4 expression extended on the stiff substrate may induce colitis-associated colorectal adenocarcinoma. These results identify tissue stiffening and mechanosignaling pathways as potential targets for IBD.

BASIC RESEARCH RELEVANCE

We developed a novel platform of culturing 2.5D intestinal organoids that closely mimics the native tissue. Using this model, we identified the influence of stiffness on ISCs and the mediating role of YAP signaling. These results, and the 2.5D gut organoid platform, could inspire mechanistic investigations into the crosstalk between mechanotransduction, metabolism, and other signaling pathways that regulate ISC function.

The intestinal stem cells (ISCs) continuously migrate on the soft basement membrane (BM) from the bottom of the crypt to the tip of the villus, differentiating into diverse types of gut epithelial cells, including goblet cells, enteroendocrine cells (EECs), tuft cells, microfold (M) cells, and enterocytes.[1] Inflammatory bowel disease (IBD), which encompasses ulcerative colitis (UC) and Crohn's disease (CD), is associated with the deterioration of gut epithelium, including loss of barrier function and alterations in the various epithelial cell populations.[2-4] Concomitantly, the excessive deposition of extracellular matrix proteins, such as collagen types I and IV, causes the BM to stiffen.[5-7] It has been shown that tissue stiffness can regulate the differentiation of mesenchymal stem cells,[8] as well as progenitor cells of the central nervous system,[9] and pancreas.[10]

Multiple investigations have also shown that modulation of stiffness can improve the spreading of 2-dimensional enteroids[11] and the viability of 3-dimensional (3D) gut organoids.[12] However, the influence of matrix stiffness on the stemness and differentiation of ISCs is not fully understood. Using 3D gut organoids cultured in an elegant designer matrix, Gjorevski et al[13] observed that stiff matrices support the maintenance of ISC stemness. This observation, however, does not align with the reduction of $LGR5^{+}$ ISCs observed in fibrotic, stiff gut.[2,4] These conflicting observations may stem from the buildup of pressure inside the hydrogel due to 3D organoid growth, which generates artificial nonphysiological compressive forces on the organoids.[13,14] Yet, it is impossible to decouple the effects of matrix stiffness from the compressive forces in the 3D matrix system. Furthermore, the impact of stiffness on the ISC differentiation trajectory is yet unknown.

Methods

Mice

Crypts were harvested from 10- to 14-week-old mice and included the following strains: wild-type C57BL/6J, *Lgr5-EGFP-IRES-CreER*,[15] conditional YAP knockout (KO), or YAP conditional overexpression (OE). To generate the conditional YAP KO mice, *CAG-rtTA3* (Jackson Laboratories, 016532) mice were mated with *tetO-Cre* (Jackson Laboratory, 006234) and $Yap^{fl/fl}$ mice.[16] To generate the conditional YAP OE mice, *tetO-YAP-GFP* mice (Jackson Laboratory, 031279) expressing mutant S112A YAP were crossbred with *Villin-rtTA*M2* mice (Jackson Laboratory, 031285). Then 1 μg/mL doxycycline (DOX) was added to induce YAP KO or OE in the organoid culture. The animals were housed and maintained on a 12-hour light/dark cycle with access to food and water ad libitum. All experimental procedures were approved by the Institutional Animal Care and Use Committee of the Massachusetts General Hospital and met the guidelines of the National Institutes of Health.

2.5-Dimensional Gut Organoid Culture

Crypts were collected from the proximal mouse small intestine with 12-cm length or from the whole colon. Both female

*** Authors share co-first authorship.**

Abbreviations used in this paper: **2.5D, 2.5-dimensional; 3D, 3-dimensional; AB, Alcian Blue; BM, basement membrane; CAC, colitis-associated colorectal adenocarcinoma; CD, Crohn's disease; cyto-YAP, cytoplasmic YAP; DMSO, dimethyl sulfoxid; DOX, doxycycline; DSS, dextran sodium sulfate; EECs, enteroendocrine cells; IBD, inflammatory bowel disease; IEGC, immature enterocyte-goblet cell; ISCs, intestinal stem cells; KO, knockout; M, microfold; nuc-YAP, nuclear YAP; OE, overexpression; OLFM4, olfactomedin-4; scRNAseq, single-cell RNA sequencing; TA, transit-amplifying; UC, ulcerative colitis; VP, verteporfin.**

Most current article

0016-5085/$36.00
https://doi.org/10.1053/j.gastro.2023.02.030

and male mice were used. No significant differences were detected between the organoids derived from the female and male mice. The intestine was washed with ice-cold phosphate-buffered saline (Corning, 21-040), and digested in ice-cold 10 mmol/L ethylenediaminetetraacetic acid (Thermo Fisher, 15575020) after cutting into 5 mm∼1 cm fragments for 40 minutes. After vigorously shaking, the crypts were collected through a 70-μm mesh (BD Falcon). About 1500 crypts were seeded on polyacrylamide gels in 35-mm dishes. The gel surface was coated with collagen IV (details in Supplementary Materials) and was flat before seeding the crypts. During the organoid growth, they deformed the surface of the soft gel, wherein the crypt region invaginated into the soft gel, forming organoids with curved indented surfaces, termed as 2.5-dimensional (2.5D) organoids. Also, 1.5 mL ENR (epidermal growth factor/Noggin/R-sponding) media/dish was added and changed every other day. Then 1 μmol/L verteporfin (VP, Sigma-Aldrich, SML0534) was added to the culture to inhibit YAP nuclear translocation. After 10-11 days in culture, the cells were fixed for immunofluorescent staining, or collected using TrypLE Express (Invitrogen, 12-605-010) for flow cytometry, transfer to 3D organoid culture in Matrigel, and single-cell RNA sequencing as described in the Supplementary Materials. Glucose uptake was tested by incubating with 2-NBDG (Cayman Chemical Company, 11046) on day 11. For measuring the level of mitochondrial superoxide, the cells were treated with 5 μmol/L MitoSOX (Thermo Fisher, M36008).

Chronic Colitis Mouse Model Induced Using Dextran Sodium Sulfate

To induce chronic colitis, wild type 8-week-old male C57BL/6J mice were given 3 cycles of dextran sodium sulfate (DSS). Each cycle included 2.5% DSS in drinking water for 1 week followed by pure drinking water for 2 weeks. Another cohort of DSS-treated animals received VP (25 mg/kg/d in dimethyl sulfoxide (DMSO); Sigma-Aldrich) or vehicle (DMSO, control) via intraperitoneal injection for 2 weeks immediately after the final dose of DSS or vehicle. After the 3 cycles of DSS, when the inflamed colon tissues were in the regenerative phase, samples were collected for stiffness measurements and immunohistochemistry as described in the Supplementary Materials.

Patient Samples

All human colon resection samples were provided by the Center for the Study of Inflammatory Bowel Disease at Massachusetts General Hospital under approved Institutional Review Board 2004P001067. The colon resection samples were obtained from 3 male patients with UC. The strictured ileum resection samples were collected from 3 male patients with CD. Sample information is provided in Supplementary Table 1. The samples were processed as described in the methods of immunohistochemistry and in situ hybridization (ISH) in the Supplementary Materials.

Statistical Analysis

The number of biological replicates or the number of animals is indicated in the figure legends. All experiments were performed with at least 3 biological replicates. For in vitro organoid culture, crypts were collected from each mouse and seeded on the gels with different stiffness. For in vivo DSS administration, littermates were randomly assigned to groups. All confidence intervals shown on the bar chats are plotted as mean ± standard deviation of the mean. Statistical analysis for significance between 2 groups was performed using the 2-tailed unpaired Student t test. One-way analysis of variance (GraphPad Prism, La Jolla, CA) assuming normal Gaussian distribution with Dunnett test was used for the multiple group comparison. $P < 0.05$ (*) was considered statistically significant.

Results

2.5D Gut Organoids Cultured on Soft Hydrogel Matrix

To better understand how stiffness influences ISC fate, we cultured gut organoids on the top surface of a polyacrylamide-hydrogel matrix with tunable stiffness (Figure 1*A*). While this platform faithfully recapitulates the anatomy of the gut epithelium, which is essentially a monolayer of epithelial cells residing on the top surface of the BM, it also allows for the exclusive manipulation of stiffness. A similar system was recently used to investigate the fundamental mechanisms contributing to the upward migration of crypt cells.[17] ISCs and crypts were harvested from mouse small intestine and seeded on top of the hydrogel matrix. *Lgr5-EGFP-IRES-creERT2* mice were used to track LGR5$^+$ ISCs. As the organoids grew, the soft hydrogel surface buckled (0.6 kPa, matching that of a healthy BM[5]), forming a 2.5D curved surface that mimics the invagination of in vivo crypts (Figure 1*B*). E-cadherin staining showed an expression concentrated at the apical surface, suggesting the establishment of epithelial polarity (Figure 1*C*). The crypt-like regions were densely populated by ISCs intermixed with large, optically dark Ulex Europaeus Agglutinin I (UEA I)$^+$ Paneth cells (Figure 1*D*). The peripheries of the crypts were surrounded by transit-amplifying (TA) cells with strong KI-67 expression, and KI-67 was also weakly expressed in LGR5^{high} ISCs. The villus-like regions were primarily populated by VILLIN$^+$ enterocytes (Figure 1*D*), with mature MUC2$^+$ goblet cells (Figure 1*E* and Alcian Blue (AB) staining in Supplementary Figure 1*A*) and Chromogranin-A$^+$ EECs being present at significantly lower numbers (Supplementary Figure 1*B*), which is consistent with the composition of the in vivo small intestinal epithelium.[18] In addition, live-cell imaging demonstrated cells in the villus-like regions having a turnover rate of approximately 3–4 days (Figure 1*F* and Supplementary Figure 1*C*, area of villus regions quantified in Figure 1*G*), like that observed in vivo. To determine how BM stiffness influences the stemness and differentiation trajectory of ISCs, the 2.5D gut organoids were cultured on hydrogel matrices of varying stiffness.

Stiffening Reduces the Number of LGR5$^+$ ISCs and Promotes Differentiation Into Mature Goblet Cells

It has been shown that healthy colon tissue has an elastic modulus around 1 kPa,[5] which is increased by at least 1

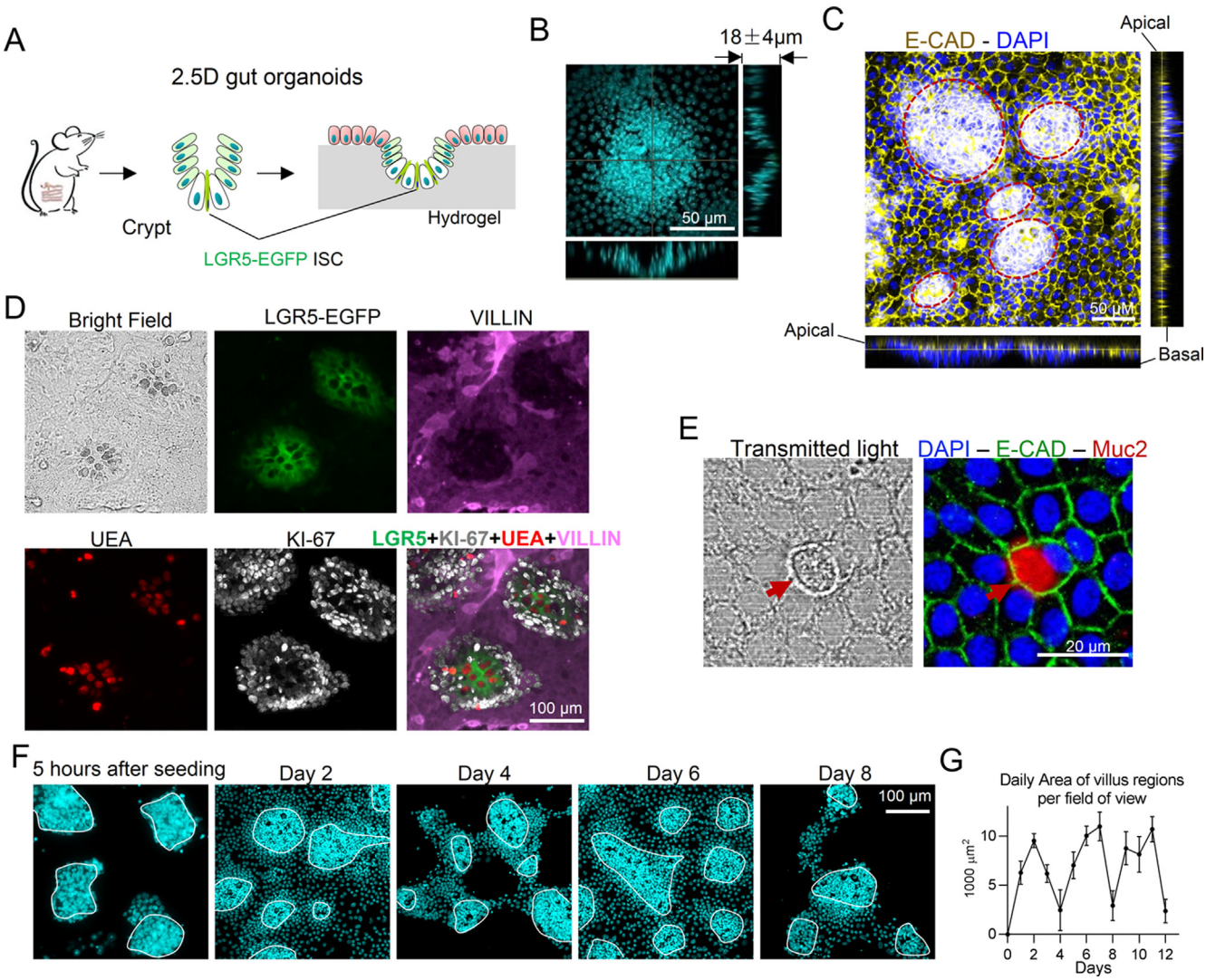

Figure 1. 2.5D gut organoids cultured on soft hydrogel matrices. (*A*) Illustration of the experimental system. (*B*) Orthogonal projection of DAPI staining showing the invagination of crypt-like region with dense nuclei. Scale bar, 50 μm. (*C*) Orthogonal projection of E-cadherin staining showing a concentrated expression at the apical surfaces (n = 3). The *red dashed lines* indicate crypt regions. Scale bar, 50 μm. (*D*) LGR5-EGFP$^+$ ISCs were intermixed with the optically dark and UEA$^+$ Paneth cells, which were surrounded by KI-67$^+$ TA cells in the crypt-like regions. The villus-like regions were populated by villin$^+$ differentiated cells (n = 3). Scale bar, 100 μm. (*E*) The confocal transmitted light image showed distinguishable morphology of MUC2$^+$ goblet cells (n = 3). Scale bar, 20 μm. (*F*) DAPI staining showed that the villus-like regions exhibited a turnover rate of 3–4 days (n = 5). The *white contour lines* indicate the crypt regions. Scale bar, 100 μm. (*G*) The area of villus regions was quantified daily. The error bars denote standard deviation.

order of magnitude in fibrotic IBD colon.[6] Thus, to determine the effects of stiffness on ISC fate, we cultured crypts on hydrogels with 3 stiffness values, ranging from 0.6 kPa–9.6 kPa. Matrix stiffening potently decreased the crypt surface area and reduced the number of LGR5-EGFP$^+$ ISCs (Figure 2*A* and 10-day live-cell image in Supplementary Figure 1*D*). The depth of the crypt invagination was also decreased (Supplementary Figure 1*E*). The stiffness-induced reduction of crypt surface area has also been reported in a recent study.[17] Flow cytometry analysis (see Methods section) further confirmed the reduction of LGR5-EGFP^{high} cells and LGR5-EGFP^{low} cells, which have been identified as ISCs and progenitor cells, respectively,[15,19] on the stiff matrix (Figure 2*B*). To further assess how stiffness impacts ISC stemness, after 11 days of culture, the cells were detached from their underlying hydrogel and transferred to grow 3D organoids within Matrigel (see Methods section). The 3D organoids generated from cells that were preconditioned on soft and medium matrices budded to form crypt-like regions with LGR5-EGFP$^+$ ISCs. Conversely, cells preconditioned on the stiff matrix generated cyst-like organoids with a significantly smaller number of buddings and negligible LGR5 expression (Figure 2*C* and Supplementary Figure 1*F*). The cyst-like organoids also displayed a substantially pronounced population of VILLIN$^+$ differentiated cells (Supplementary Figure 1*G*). Thus, the loss of ISC stemness

caused by stiffening was persistent and did not recover after transferring into Matrigel. This observation indicates that the impacts of gut stiffening are memorized by ISCs and can persist even during the remission period of IBD.

Compared with the well-studied role of LGR5 in activating WNT signaling pathway, the functions of another stem cell marker, olfactomedin-4 (OLFM4), are not yet fully understood. It is demonstrated that OLFM4 is a target of the NOTCH signaling,[20] which can also negatively regulate WNT/β-catenin activation.[21] Here, we found that the expression and distribution of OLFM4 was also strongly influenced by matrix stiffness (Figure 2*A*). On the medium and stiff substrates, OLFM4^{+} cells can replace the LGR5^{+} ISCs and became dominant in the crypt region (Supplementary Figure 1*H*) and extended into villus-like regions (Figure 2*A*).

Live-cell imaging on the soft matrix depicts how the LGR5-EGFP^{+} ISCs divide and differentiate into large, optically dark Paneth cells (Supplementary Figure 1*I* and Video 1). The generation of Paneth cells is thought to be critical for long-term maintenance of the ISC niche and stemness.[22] Intriguingly, the long-term live-cell imaging demonstrated that, on the stiff matrix, the LGR5^{-} cells in the villus-like regions directly differentiated into Paneth cells around which new crypt-like regions formed (Figure 2*D* and Video 2). In the bright-field images, the crypt regions were easily distinguishable by the presence of the large and dark Paneth cells (Supplementary Figure 1*J*). Moreover, other cells in the crypt regions were much denser and smaller than the cells in the villus regions. The incidence of these new crypt formations was approximately 3-fold higher on stiff matrix compared with soft matrix (Supplementary Figure 1*K*). Considering the absence of LGR5 expression in the villus-like regions, this result suggests OLFM4^{+} cells may give rise to the formation of the new crypts.

Matrix stiffness also profoundly impacted the differentiation trajectory of the ISCs. Increasing the stiffness significantly reduced the populations of KI-67^{+}–proliferating cells, the Lysozyme^{+} Paneth cells, the enterocytes (marked by VILLIN and intestinal alkaline phosphatase, ALPI), and the Chromogranin-A^{+} EECs (Figure 2*E* and Supplementary Figure 2*A*). In contrast, the marker of secretory progenitor cells, delta like canonical notch ligand 1 (DLL1), and the goblet cell marker, MUC2, were increased (Figure 2*E* and Supplementary Figure 2*A*). The side views consistently showed that increasing stiffness decreased the expression of KI-67 and LGR5 in the invaginated crypt regions and the VILLIN expression and promoted the expression of MUC2 (Supplementary Figure 2*B*). Examination of the MUC2 staining images demonstrated the presence of 2 distinct cell populations on the stiff substrate: those with strong MUC2 expression (ie, MUC2^{hi}) and a population with weak MUC2 expression (ie, MUC2^{low}; Figure 2*E*). Intriguingly, costaining for AB, which marks mature goblet cells, and MUC2 demonstrated that only the MUC2^{hi} cells were AB-positive, suggesting that the MUC2^{hi} cells were mature goblet cells (Supplementary Figure 2*C*). Consistent with this observation, there were approximately a 6-fold increase in the populations of both MUC2^{hi} and AB+ cells on the stiff substrate (Figure 2*E* and Supplementary Figure 2*A*). The MUC2^{low} cells simultaneously expressed ALPI (Supplementary Figure 2*D*) and stem cell marker, OLFM4 (Supplementary Figure 2*E*). We referred to these cells as immature enterocyte-goblet cells (IEGCs), where "immature" refers to the coexpression of multiple cell type markers. Flow cytometry analysis (see Methods section) confirmed the reduction of KI-67^{+}–proliferating cells (Figure 2*F*) and Paneth cells (CD24^{high}, C-KIT^{+} and SSC^{high}; Figure 2*G*) on stiff matrix.

Notably, a similar self-organizing, crypt-villus structure and stiffness-dependent phenotype are also observed when flow cytometry–sorted single LGR5^{+} cells were cultured, wherein stiffening decreased the populations of LGR5^{+} and VILLIN^{+} cells, and increased MUC2^{+} cells (Supplementary Figures 2*F*–*I*). We also performed analogous analyses on the organoids derived from colon crypts. Increasing substrate stiffness diminished the population of LGR5^{+} ISCs and KI-67^{+}–proliferating cells (Supplementary Figure 3*A*–*C*). Furthermore, the expression of the enterocyte marker, ALPI, was reduced, whereas MUC2 expression was increased on the stiff substrate (Supplementary Figure 3*D* and *E*). Thus, the influence of stiffness on colon ISCs is similar to what we observed in small intestinal ISCs.

The schematic in Figure 2*H* summarizes the influence of stiffening on the fate of ISCs: in the crypt-like regions, stiffening led to a loss of LGR5^{high} ISCs and reduced the population of LGR5^{low}, KI-67^{+} TA progenitor cells. In the villus-like regions, stiffening led to the replacement of the VILLIN^{+} mature enterocytes by MUC2^{+}, VILLIN^{+}, and OLFM4^{+} IEGCs and mature goblet cells.

Stiffness Differentially Regulates YAP in Crypts and Villus Regions

We asked whether the mechano-transducer, YAP, plays a role in the regulation of ISC fate by stiffness. On the soft matrix, YAP expression was exclusively observed in the crypt region, and increasing the stiffness led to a significant increase in YAP expression and nuclear translocation across both crypt- and villus-like regions (Figure 3*A* and *B*). Consistently, stiff substrate also promoted the YAP nuclear translocation of colon organoids (Supplementary Figure 3*F* and *G*). To better distinguish the expression patterns of nuclear YAP (nuc-YAP) and cytoplasmic YAP (cyto-YAP), and because YAP phosphorylation inhibits its nuclear translocation,[23] we performed immunofluorescence of nonphosphorylated nuc-YAP and Ser-127 phosphorylated cyto-YAP, respectively. We observed that nuc-YAP expression was increased across both the crypt- and villus-like regions on stiff matrix (Figure 3*C*). In contrast, cyto-YAP exhibited a strong region-dependent expression pattern, wherein it was decreased by stiffening in the crypt-like regions but increased in the villus-like regions (Figure 3D).

Stiffness-Dependent Expressions of Nuc-YAP and Cyto-YAP Play Divergent Roles in Determining the Fate of ISCs

To assess how the stiffness-dependent YAP expression and sequestration impact ISC fate, we manipulated YAP via

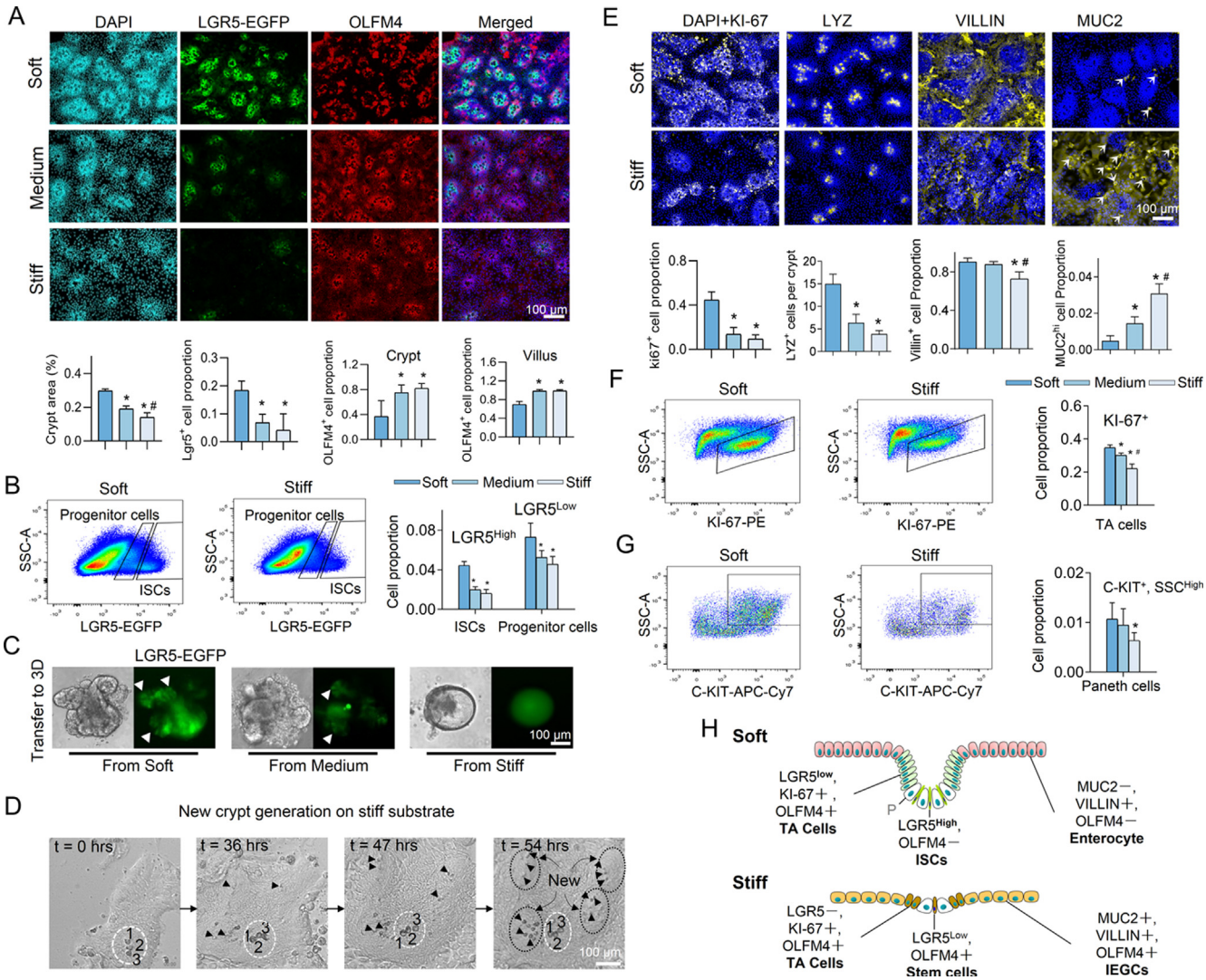

Figure 2. Stiffness determines the fate of ISCs. (*A*) Increasing the matrix stiffness from soft (0.6 kPa) to medium (2.4 kPa) to stiff (9.6 kPa) reduced the size of the crypt-like regions with dense nuclei and decreased the expression of LGR5. Stiffening also extended the OLFM4$^+$ cells into villus-like regions. Scale bar, 100 μm. The crypt surface area was quantified as a proportion of total area, the number of LGR5$^+$ cells as a proportion of total cells, and the number of OLFM4$^+$ cells as a proportion of total cells in the crypt regions and in the villus regions (n = 3–5). (*B*) Flow cytometry analysis showed that stiffening decreased LGR5^{high} ISCs and LGR5^{low} progenitor cells (n = 3). (*C*) The 3D organoids derived from the soft and medium matrix budded with LGR5-EGFP$^+$ ISCs (*white arrows*). The 3D organoids derived from the stiff matrix grew more like LGR5-EGFP$^-$ cysts (n = 3). Scale bar, 100 μm. (*D*) Live-cell imaging demonstrates the generation of new crypts in the villus-like region of the stiff substrate (Video 2). At t = 0 h, only 1 crypt is visible (*white dashed ellipse*) surrounded by the villus region. The large and optically dark Paneth cells (enumerated by 1, 2, and 3) are used as a point of reference. At t = 36 h, new Paneth cells (*black arrows*) appear within the villus region. At t = 47 h, more Paneth cells are visible within newly formed crypts. At t = 54 h, 4 new, fully formed crypts (*black dashed ellipses*) are visible. Scale bar, 100 μm. (*E*) Stiffening decreased the expression of KI-67, Lysozyme (LYZ), and VILLIN, but increased MUC2 (n = 3–5). Scale bar, 100 μm. KI-67$^+$, VILLIN$^+$ cells, and MUC2^{high} cells (*arrows*) were, respectively, quantified as their proportion of total cells. LYZ$^+$ cells is quantified as cell number per crypt. Flow cytometry analysis showed that stiffening decreased KI-67$^+$ TA cells (*F*; n = 3) and Paneth cells (*G*; n = 6). (*H*) Schematic summarizing the impact of stiffening on all cell types. P, Paneth cell. *vs soft and #vs medium; $P < 0.05$ (one-way analysis of variance). The error bars denote standard deviation.

transgenic mouse models with DOX-inducible conditional YAP knockout (*CAG-rtTA3*; *tetO-Cre*; *Yap*$^{flox/flox}$) or YAP overexpression (OE: *villin-rtTA*M2*; *tetO-YAP-GFP*) (see Methods section). Then, crypts were harvested from naïve animals and the transgene was induced in vitro. Also, YAP inhibitor, VP, was used to suppress YAP nuclear translocation.[24] We observed that LGR5$^+$ ISCs were YAP negative, and YAP expression was inversely correlated with LGR5 expression (Figure 4*A*, as quantified in Figure 4*D*). YAP OE on the soft substrates led to the disappearance of the crypt-like regions (Figure 4*B*), causing a shift toward the stiff matrix-like phenotypes. Conversely, VP administration

on the stiff matrix led to the formation of large crypt-like regions and restored LGR5 expression (Figure 4*C*, as quantified in Figure 4*D*), bestowing the soft matrix-like phenotypes. These observations demonstrated that YAP activation inhibits LGR5 expression.

The goblet cell marker, MUC2, was strongly correlated with YAP nuclearization (Figure 4*E*, as quantified in Figure 4*H*). Comparing the phenotypes between the YAP OE on the soft substrate and the VP administration on the stiff substrate demonstrates that increasing nuc-YAP expression by YAP OE promoted MUC2 (Figure 4*F* and Supplementary Figure 4*A*), whereas decreasing nuc-YAP by VP suppressed MUC2 (Figure 4*G*, as quantified in Figure 4*H*).

On the other hand, OLFM4 expression in the villus region exhibited strong correlation with cytoplasmic YAP, wherein induction of OLFM4 on medium stiffness was associated with the appearance of cytoplasmic YAP expression (Figure 4*I*). Consistently, compared with the medium substrate, the reduction in cytoplasmic YAP on stiff substrate caused by the enhanced YAP nuclearization was associated with the reduction in OLFM4 expression (Figure 4*I*, as quantified in Figure 4*L*). Meanwhile, augmentation of cytoplasmic YAP by both YAP cOE (Figure 4*J* and Supplementary Figure 4*B*) and VP administration (Figure 4*K*) persistently increased the expression of OLFM4, confirming that cyto-YAP positively regulates OLFM4 (as quantified in Figure 4*L*).

YAP KO on both soft and stiff substrates led to the loss of villus-like regions (Supplementary Figure 4*C*). The leftover crypt-like regions were enriched with Paneth cells and were negative for nuc-YAP and cyto-YAP, as well as MUC2, OLFM4, and VILLIN (Supplementary Figure 4*D* and *E* as quantified in Supplementary Figure 4*F*). These data demonstrated the indispensability of YAP to the differentiation of ISCs and the generation of villi.

Here, the combination of mechanical, genetic, and pharmacologic manipulation of YAP expression and sequestration discriminate the functional roles of nuc-YAP and cyto-YAP in the regulation of ISC stemness and differentiation (ie, YAP is indispensable for ISC differentiation and villus generation), and stiffening-induced YAP nuclearization suppresses the population of $LGR5^+$ ISCs and drives the differentiation into goblet cells, whereas cyto-YAP drives the differentiation toward $OLFM4^+$ cells.

Stiffness-Regulated Transcriptional Signatures of ISCs and Their Differentiated Progeny

To provide a comprehensive map of how stiffness impacts ISCs and their differentiated progeny at the transcriptional level, we performed single-cell RNA sequencing (scRNAseq) analysis. The single-cell expression profiles of our 2.5D gut organoids were clustered into 13 cell groups (Figure 5*A*, Supplementary Table 2). Thirty principal components were selected for the dimensional reduction based on their statistical significance ($P < 0.05$). Cluster annotation using known epithelial marker genes[25] revealed that all the different types of progenitors and differentiated gut epithelial cells are present in the in vitro system (Figure 5*A* and *B*, Supplementary Figure 5). The trajectory inference using Partition-based graph abstraction[26] demonstrated a trajectory from stem cells and TA cells to the progenitor cells to the differentiated cell populations (Supplementary Figure 6). Clustering was consistent across the biological triplicated samples for both soft and stiff conditions (Supplementary Figure 7*A*). IEGCs simultaneously expressed mild levels of marker genes for stemness, enterocytes, and goblet cells (Figure 5*B*, Supplementary Figure 2*D* and *E*). scProportionTest analysis (see Methods section) also confirmed the effects of stiffening on the ISC differentiation trajectory, including a 25% and 42% reduction in ISCs and tuft cells, respectively (Figure 5*C*). Goblet cells, M cells and IEGCs were increased by 28%, 24% and 25%, respectively. Differential expression analysis (Supplementary Table 3) and immunofluorescence imaging showed extensive and widespread expression of another goblet cell marker, Trefoil factor 3, across the whole villus region on the stiff substrate (Figure 5*D*).

We next assessed the expression levels of the known YAP–up-regulated and –down-regulated genes previously curated by Gregorieff et al.[27] The top 18 YAP–down-regulated genes showed consistently greater expression in both enterocytes and enterocyte progenitors, whereas the top 17 YAP–up-regulated genes showed greater enrichment in goblet cells, IEGCs, and M cells (Figure 5*E*, Supplementary Figure 7*B*). Furthermore, the gene expressions of *Id2*, *Birc5*, and *Areg*, which are downstream of nuc-YAP,[28] were significantly increased on stiff matrix (Supplementary Figure 7*C*). Pathway enrichment analysis also revealed an up-regulation of mechanotransduction signaling pathways, including actin cytoskeleton, focal adhesion, and tight junctions, potentially contributing to YAP activation (Supplementary Figure 7*D*). These results further corroborate that matrix stiffening activates YAP, which in turn mediates the differentiation of ISCs toward goblet cells, as opposed to enterocytes.

Stiffening suppressed the gene expression of *Lgr5* and *Sox4*, a WNT/β-catenin agonist,[29] in ISCs (Supplementary Figure 7*E*), consistent with the loss of stemness on stiff matrix. Furthermore, *Hes1*, a Notch pathway target gene,[30] was also down-regulated on stiff matrix (Supplementary Figure 7*E*). HES1 inhibition is known to promote goblet cell differentiation at the expense of enterocytes,[31] which is also in accordance with stiffening-enhanced goblet cell differentiation. In addition, the PROGENy activity scores (see Methods section)[32] across all the cells demonstrated that the WNT, transforming growth factor beta (TGF-β), and MAPK pathways were significantly activated on the soft substrate. Conversely, tumor necrosis factor-related apoptosis-inducing ligand (TRAIL) pathways were significantly activated on the stiff substrate (Supplementary Figure 8*A*). The PROGENy activity scores of each cell population showed that ISCs and enterocyte progenitor cells contributed to the different WNT activity on the soft vs stiff substrate; enterocyte progenitor cells and M cells to the different TGFb activity; ISCs, enterocyte progenitor cells, and goblet cells to the different activities of TRAIL and MAPK pathways (Supplementary Figure 8*B*).

The scRNAseq analysis further suggested that stiffening strongly influences the metabolic activity and demand of

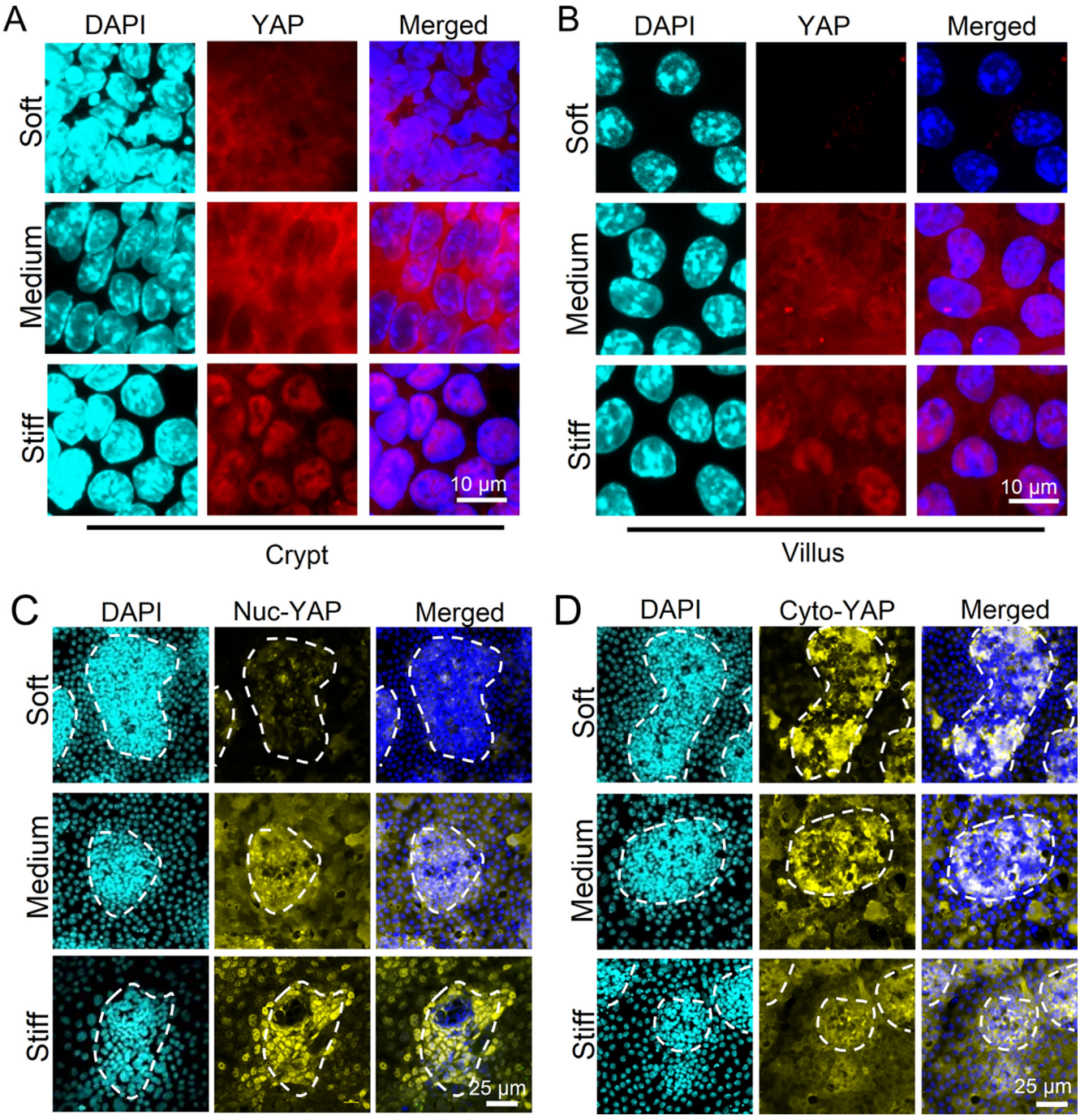

Figure 3. Influence of stiffness on YAP expression and sequestration in crypt-like and villus-like regions. On the stiff gel, nuclear localization of YAP was shown on both crypt (*A*) and villus (*B*) regions. In villus regions, cyto-YAP expression was absent on the soft matrix and highly expressed on the medium matrix (*B*) (n = 3). Scale bar in (*A*) and (*B*), 10 μm. (*C*) The nonphosphorylated nuc-YAP was increased by stiffening and showed clear nuclear localization on the stiff matrix (n = 5). Scale bar, 25 μm. (*D*) The Ser 127 phosphorylated cyto-YAP was decreased by stiffening in the crypt-like regions, but increased in the villus-like regions (n = 5). Scale bar, 25 μm.

cells, the hallmark of which was increased carbon metabolism (from pathway enrichment analysis; Figure 5*F*, Supplementary 7*F*). In particular, the glycolytic pathway, tricarboxylic acid cycle, and oxidative phosphorylation pathway were all up-regulated on stiff substrate (Figure 5*F* and the corresponding genes in Supplementary Table 4), suggesting augmented glucose use and catabolism. The direct assessment of glucose uptake, mitochondrial reactive oxygen species (MitoSOX, direct byproducts of oxidative phosphorylation) (Figure 5*G*) and expression of the glucose transporter 2 (Figure 5*H*) corroborated with the high demand of glucose on stiff matrix. Intriguingly, inhibiting glucose uptake on stiff matrix via the pan-class I glucose transporter inhibitor, Glutor, increased crypt size and

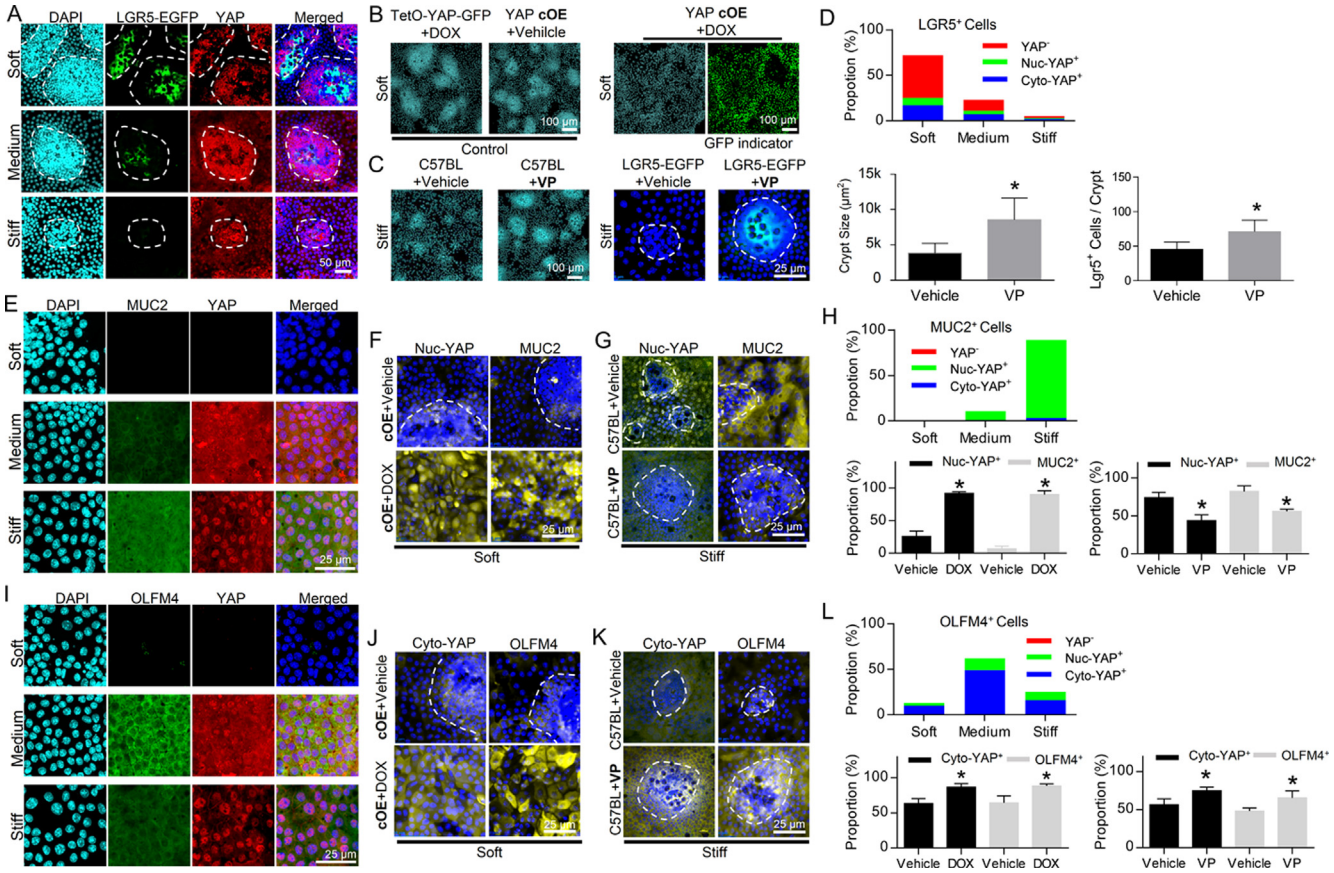

Figure. 4. Stiffness regulates ISC fate via YAP. The fate of ISCs was manipulated via conditional YAP knockout (cKO), conditional YAP overexpression (cOE), and VP. (*A*) Lgr5-EGFP^{+} ISCs were YAP^{-} and disappeared when YAP expression was positive. The *white dashed lines* trace the crypt-like regions (n = 3). Scale bar, 50 μm. (*B*) YAP cOE led to the loss of the crypt-like regions on the soft matrix. TetO-YAP-GFP cells with DOX and YAP cOE cells without DOX served as control groups. Scale bar, 100 μm. (*C*) VP administration increased the size of the crypt-like regions and restored LGR5-EGFP expression on the stiff matrix. Scale bars, 100 μm for the C57BL mouse group and 25 μm for the LGR5-EGFP mouse group. (*D*) Quantification of (*A*, *B*, and *C*) shows the proportions of YAP^{-}, nuc-YAP^{+}, and cyto-YAP^{+} cells in LGR5^{+} cells as well as impacts of VP on crypt size and number of LGR5^{+} cells per crypt. (*E*) MUC2 was highly expressed in cells with intense YAP nuclear localization in villus regions (n = 3). Scale bar, 25 μm. (*F*) YAP cOE on soft substrate increased both nuc-YAP and MUC2. Scale bar, 25 μm. (*G*) VP administration on stiff substrate decreased both nuc-YAP and MUC2. Scale bar, 25 μm. (*H*) Quantification of (*E*, *F*, and *G*) shows the proportions of YAP^{-}, nuc-YAP^{+}, and cyto-YAP^{+} cells in MUC2^{+} cells and the impacts of YAP OE and VP on the proportions of nuc-YAP^{+} and MUC2^{+} cells in total cells. (*I*) OLFM4 expression was highly correlated with cytoplasmic YAP stained with total YAP in villus regions (n = 3). Scale bar, 25 μm. Both YAP cOE on soft substrate (*J*) and VP administration on stiff substrate (*K*) persistently increased cyto-YAP and OLFM4. Cyto-YAP was stained with Ser 127 phosphorylated YAP. Scale bar in (*J*) and (*K*), 25 μm. (*L*) Quantification of (*I*, *J*, and *K*) shows that the proportions of YAP^{-}, nuc-YAP^{+}, and cyto-YAP^{+} cells in OLFM4^{+} cells and the impacts of YAP OE and VP on the proportions of cyto-YAP^{+} and OLFM4^{+} cells in total cells. *$P < 0.05$ (Student *t* test). The error bars denote standard deviation.

decreased MUC2 expression, resulting in a shift toward soft matrix-like phenotypes (Figure 5*I*). These results demonstrate that matrix stiffening potently augments glucose metabolism in ISCs and their progeny, and that the resultant metabolic rewiring plays a critical role in mediating the effects of stiffness on ISC fate.

Colon Stiffening Triggers ISC Remodeling in Murine Model of Colitis

To verify our in vitro observations on the role of stiffness in determining ISC fate, we used a mouse model of chronic colitis, in which the animals were administered 3 weeks of DSS (or water as control), each of which was interspersed by 2 weeks of recovery.[33] Furthermore, another cohort of DSS-treated animals received VP (or DMSO as control) throughout the final 2 weeks of recovery (see Methods section), during which the epithelium was regenerated from inflammation-induced damage (Figure 6*A*). We confirmed that VP or DMSO administration in the no-DSS control groups did not induce detectable changes. In the colitis model, the colon stiffened and thickened (Figure 6*B*). Similar to our in vitro observations, the stiffened colitis colon was associated with increased nuc-YAP expression, and VP administration in the DSS-induced colitis mice suppressed nuc-YAP expression and increased cyto-YAP

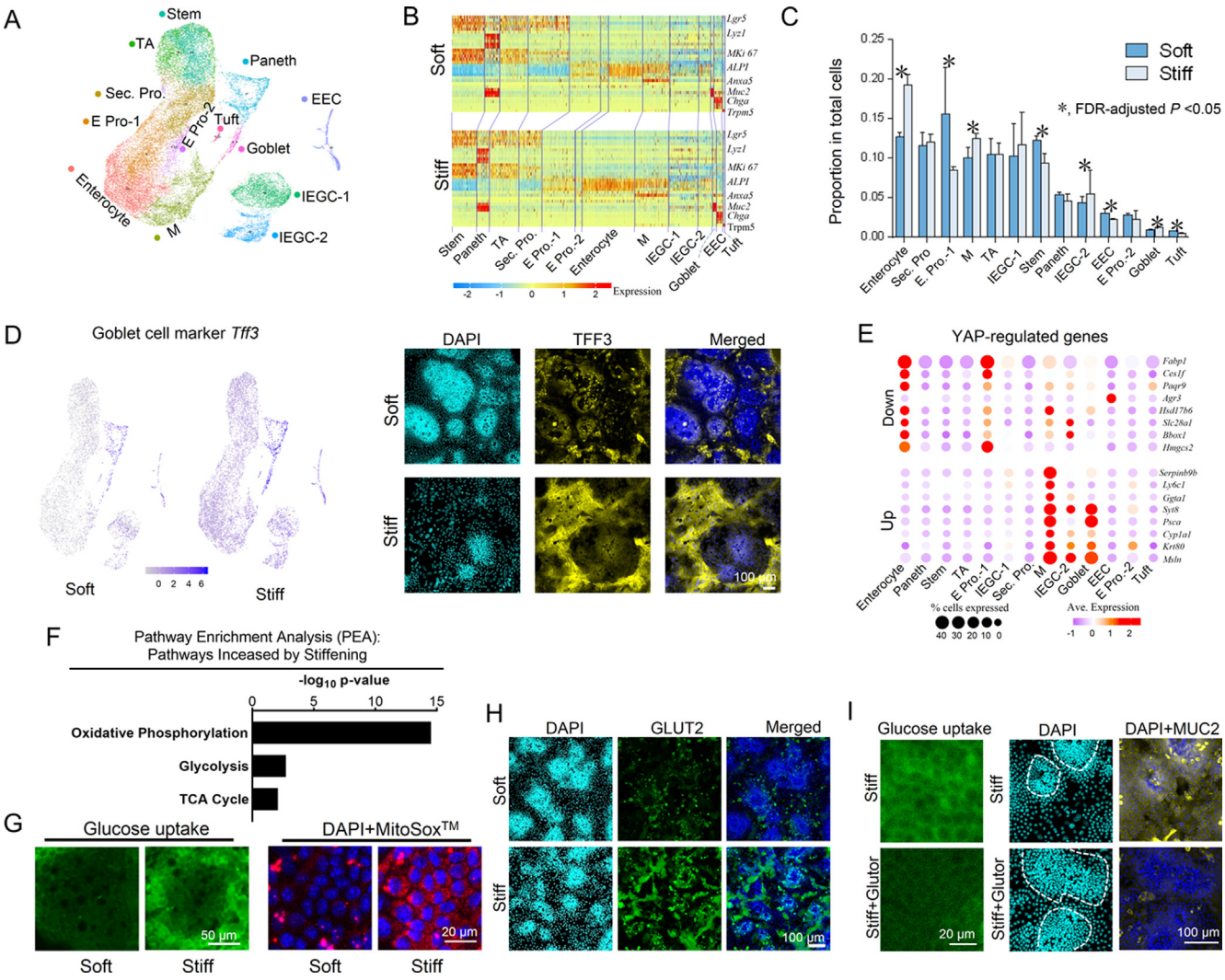

Figure 5. scRNAseq of 2.5D gut organoids. (*A*) Uniform manifold approximation and projection (UMAP) plot with cell clusters (marked by *color*) including ISCs and differentiated cells. Sec, secretory; Pro, progenitor; E, enterocyte; M, microfold. (*B*) Heat map for marker genes of each cell type (Supplementary Figure 5). (*C*) The differences of the proportions of each cell type between the soft and stiff matrices analyzed using the scProportionTest tool. (*D*) Differential expression analysis and immunofluorescence showed that expression of Trefoil factor 3 gene was higher on the stiff matrix compared with the soft matrix. Scale bar, 100 μm. (*E*) Genes down-regulated by YAP were highly expressed in the enterocyte and E pro-1 clusters; genes up-regulated by YAP were highly expressed in goblet cells, IEGC-1, and M cells. (*F*) Pathway enrichment analysis (PEA) demonstrates that the metabolic pathways involved in glucose uptake and catabolism, including oxidative phosphorylation, glycolysis, and tricarboxylic acid (TCA) cycle, are more enriched on the stiff substrate. (*G*) Glucose uptake and mitochondrial activity assays, using 2-NBDG Administration and Mitosox measurement, respectively, demonstrate that stiffening increases glucose uptake and catabolism. Scale bars, 50 μm for the glucose uptake images and 20 μm for the Mitosox images. (*H*) Glucose transporter 2 (GLUT2) expression was greater on stiff matrix compared with soft matrix. Scale bar, 100 μm. (*I*) On stiff matrix, the administration of the pan-class I GLUT inhibitor, Glutor, inhibited the uptake of glucose analog 2-NBDG, increased the crypt size, and decreased MUC2 expression. Scale bars, 20 μm for the glucose uptake images and 100 μm for the MUC2 staining images. n = 3 for *A-I*.

(Figure 6*C*). The YAP expression pattern was consistent across the entire colon epithelium (Supplementary Figure 4*G*). Consistently, LGR5 expression decreased in the colitis colons, and was recovered after VP administration (Figure 6*D*). Also, the extensive presence of goblet cells exhibited in the brush borders of the colitis colon and was inhibited after VP administration (Figure 6*E*). Consistent with our in vitro observations, VP administration in colitis mice potently recovered the LGR5 expression and suppressed both nuc-YAP expression and goblet cell differentiation, reversing the effects of colon stiffening. In addition, VP administration mitigated the body weight loss and colon thickening of DSS-induced colitis mice (Supplementary Figure 4*H*).

Stiffness-Induced ISC Remodeling in Human IBD Patients

To determine the extent to which the stiffening-induced remodeling of our gut organoids and murine gut epithelium

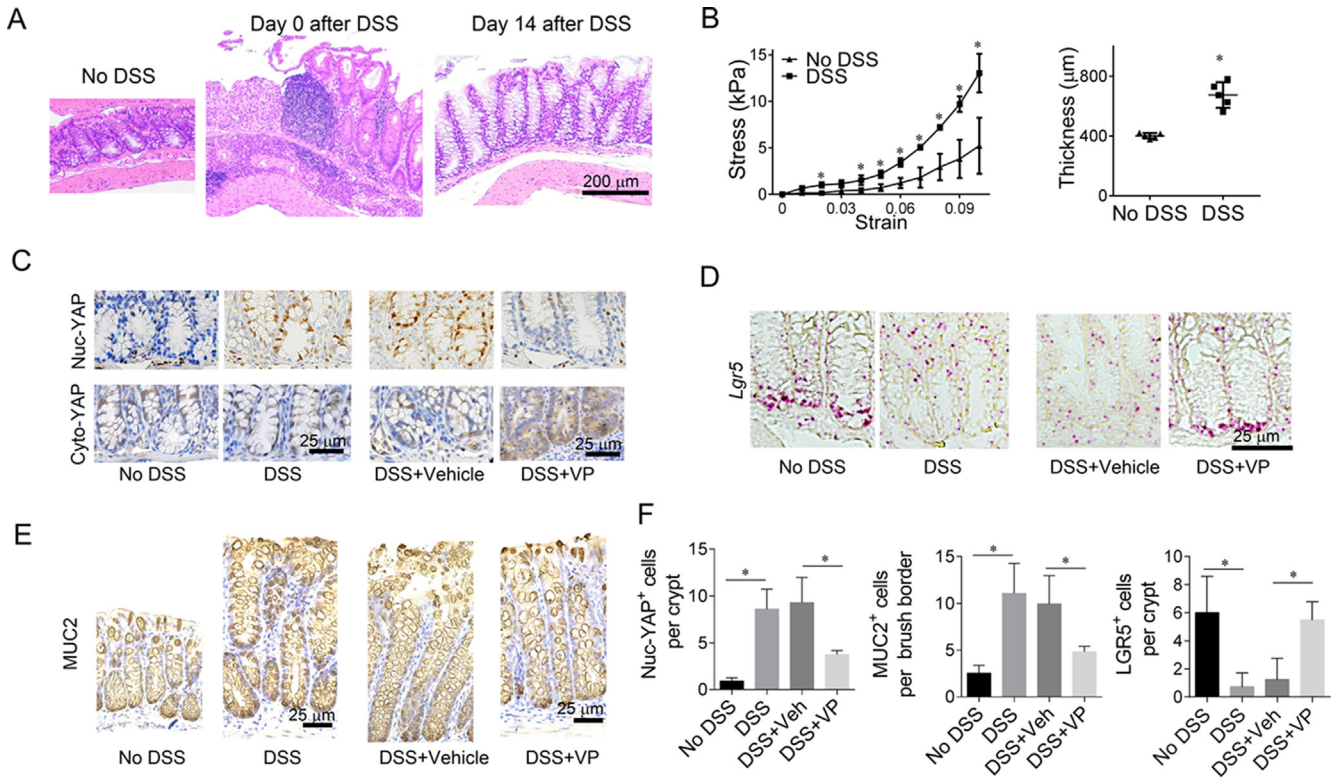

Figure 6. Stiffness regulates ISC fate in this chronic colitis mouse model. (*A*) H&E staining shows that the colon epithelium with severe damage on Day 0 was significantly regenerated on Day 14. Scale bars, 200 μm. (*B*) Colon stiffened (n = 3) and thickened (n = 6) in the DSS-induced colitis group compared with the control group without DSS. Methods for the measurement of colon stiffness and thickness are in the Methods section. (*C*) As shown in immunohistochemistry (IHC), nuc-YAP stained with nonphosphorylated YAP increased in the DSS groups compared with no DSS control. VP treatment caused a reduction of nuc-YAP and increased cyto-YAP expression. Scale bars, 25 μm. (*D*) In situ hybridization (ISH) showed that *Lgr5* expression was suppressed in DSS ground and was recovered after VP treatment. Scale bars, 25 μm. (*E*) MUC2 expression (IHC) was augmented in the colon brush border of DSS groups, and was decreased after VP administration. Scale bars, 25 μm. (*F*) Quantification of nuc-YAP$^+$ cells and LGR5$^+$ cells per crypt and MUC2$^+$ cells per colon brush border. n = 3–6. *$P < 0.05$ (Student *t* test). The error bars denote standard deviation.

resembles that of human patients with IBD, we analyzed scRNAseq data generated from colon resection samples of patients with IBD and healthy individuals.[34] The human single cell profiles were clustered into 10 epithelial cell subsets that were annotated using known marker genes (Supplementary Figure 9*A* and *B*). IBD was associated with a decrease in patients' ISC and enterocyte populations, and an increase in goblet cells (Figure 7*A*, Supplementary Figure 9*C* with and without accounting for sample size, respectively), which are consistent with the phenotypes of substrate stiffening observed in vitro. Pathway enrichment analysis demonstrated strong activation of the pathways involved in extracellular matrix biosynthesis (including *COLLAGEN I* and *IV*) in IBD, which is indicative of increased fibrosis and stiffening (Figure 7*A*). Concomitantly, *WNT* signaling was suppressed in the ISC population of patients with IBD (Figure 7*A* and Supplementary Figure 9*D*). In addition, there was potent activation of the mechanosignaling pathway, including *INTEGRIN*, *YAP*, and *TEAD* (the primary transcription factors for YAP), in both the ISCs and the goblet cells of patients with UC, but not in the enterocytes (Supplementary Figure 9*E*). In agreement with this observation, the established YAP–up-regulated genes[27] were enriched in both ISC and goblet cell populations of IBD colon (Figure 7*A*). The scRNAseq analysis of the human IBD and healthy samples identified similar key features compared with those observed from the in vitro organoids. Most notably, in patients with IBD the population of ISCs decreased and goblet cells increased. In addition, YAP signaling pathway is up-regulated and Wnt signaling pathway is suppressed in ISCs.

Histomorphometric analysis of human colon tissues demonstrated thickening of the BM and lamina propria, the disappearance of enterocyte brush borders (Figure 7*B*), and excessive collagen deposition and fibrosis (Figure 7*C* and *D*) in IBD. The number of KI-67$^+$–proliferating cells and LGR5$^+$ ISCs was significantly decreased in IBD samples (Figure 7*E*). Conversely, OLFM4 expression was increased and extended into the apical surface (Figure 7*F*), consistent with previous reports.[35] Notably, in extremely fibrotic and strictured ileum samples, the invaginated ISC niche-crypts nearly disappear and only pieces of the villi remain, resembling the stiffness-reduced size of the crypt and loss of ISCs (Figure 7*G*). Meanwhile, numerous ectopic crypts have formed, resembling the stiffness-induced new crypt formation, which, despite

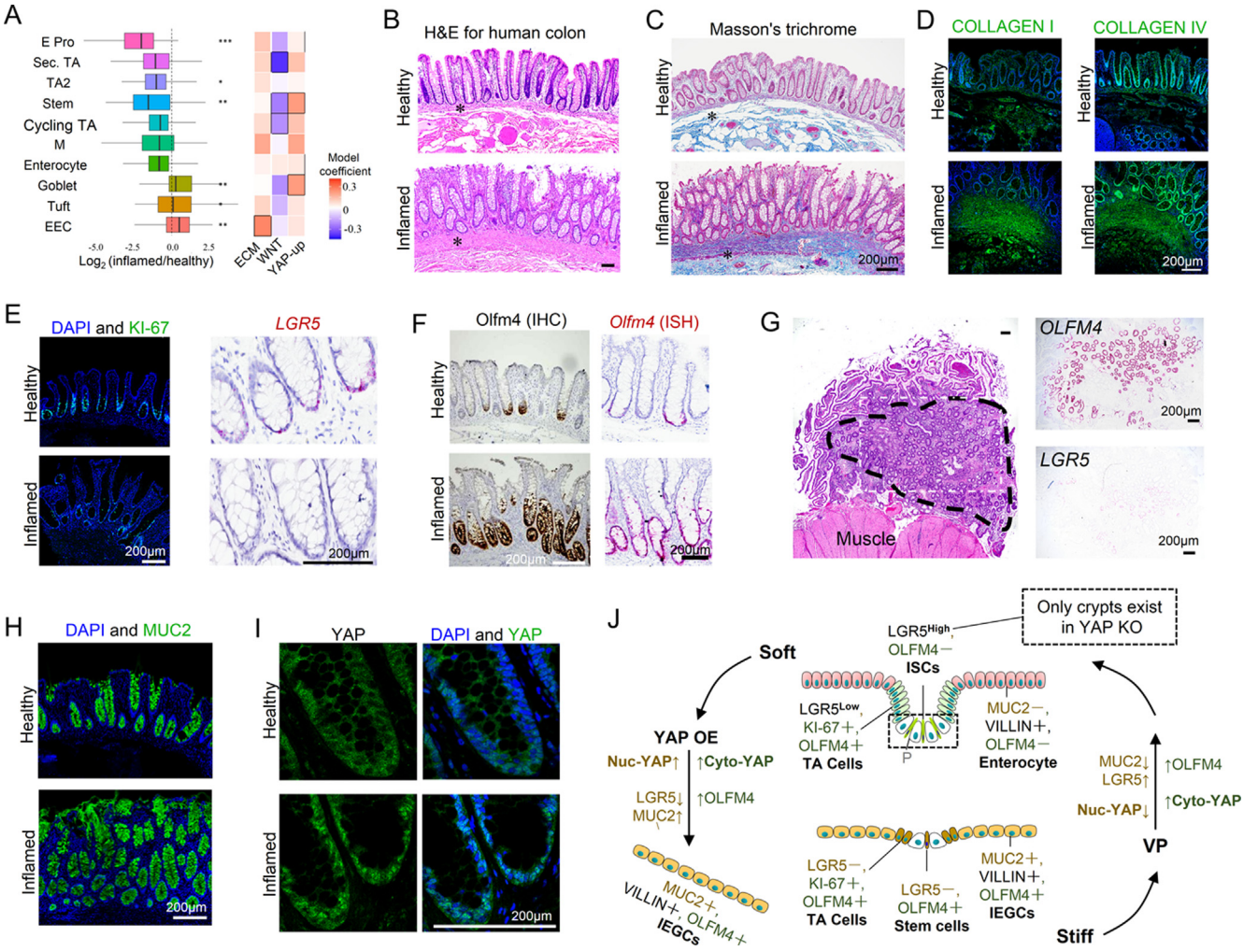

Figure 7. Stiffness regulates ISC fate in human patients with IBD. (*A*) scRNAseq analysis showed a decrease in ISC population and an increase of goblet cell population in human IBD colon. *$P < 0.05$; **$P < 0.01$; ***$P < 0.001$. Pathway enrichment analysis showed that in IBD samples, *WNT* signaling is suppressed in ISCs, YAP up-regulated genes are highly expressed in ISCs and goblet cells, and ECM biosynthesis is activated in EECs. *Boxes outlined in black* represent $P < 0.05$ for the linear mixed model and $P < 0.05$ for pathway enrichment (see Methods section). (*B*) H&E staining of human colon tissues shows thickening of the BM and lamina propria (*asterisks*). Masson's trichrome staining (*C*) and staining of COLLAGEN I and IV (*D*) reveal fibrosis of lamina propria. Scale bars in (*C*) and (*D*), 200 μm. (*E*) KI-67$^+$–proliferating cells and LGR5$^+$ ISCs were decreased, and (*F*) OLFM4$^+$ cells were increased in the IBD samples. Scale bars in (*E*) and (*F*), 200 μm. (*G*) In a large area (*outside the dashed line*) of the strictured ileum (extreme fibrosis), the invaginated ISC niche-crypts nearly disappear and only pieces of the villi remain. Numerous ectopic crypts (*inside black dashed line*) have formed and expressed strong OLFM4 and weak LGR5. Scale bar, 200 μm. (*H*) MUC2+ goblet cells increased in the inflamed colon. (*I*) YAP showed greater expression and nuclear localization in the IBD colon (n = 6). Scale bar, 200 μm. (*J*) Schematic describing the stiffening-dependent ISC fate, showing that stiffness regulates ISC fate via YAP, and YAP OE transforms the soft-matrix phenotypes into the stiff-matrix phenotypes, and VP does the reverse. *Yellow* indicates regulation by nuc-YAP. *Green* indicates regulation by cyto-YAP.

negligible LGR5 expression, exhibited strong OLFM4 expression (Figure 7*G*). Like our in vitro observations, MUC2$^+$ goblet cells were overwhelmingly present in IBD colon compared with healthy tissues (Figure 7*H*). Notably, there was strong YAP expression and nuclear localization in the IBD samples (Figure 7*I*). The scRNAseq and histology data from human patients with IBD strongly complemented our in vitro observations, demonstrating that gut stiffening is associated with strong YAP up-regulation, loss of ISCs, extension of OLFM4 expression, and enhanced differentiation toward goblet cells. Together, these results suggest that stiffness plays a direct and critical role in epithelial remodeling in IBD.

Therefore, on the basis of our complementary in vitro and in vivo observations, we have demonstrated that stiffness regulates ISC fate via YAP, wherein the stiffness-induced loss of LGR5$^+$ ISCs and the differentiation toward MUC2$^+$ goblet cells is mediated by nuc-YAP. On the other hand, cyto-YAP drives the differentiation toward OLFM4$^+$ cells (Figure 7*J*).

Discussion

Previous studies with the purpose of designing in vitro 3D matrices for 3D organoid culture showed that the stiffer matrix promoted ISC expansion and the softer matrices enhanced crypt budding and ISC differentiation.[13] However, these phenotypes are not consistent with the reduction of ISCs in the fibrotic stiff intestine in IBD.[2,4] This could be due to challenges associated with tuning stiffness in 3D hydrogel matrices, which causes secondary effects such as increased pressure. Furthermore, considering that the in vivo intestinal epithelium has a monolayer structure with an open lumen, our systems represent a higher-physiological relevance, particularly in the context of studying cell-matrix biophysical interactions. Moreover, the influence of stiffness on the differentiation trajectory of ISCs is still not clear. Using our 2.5D organoids, we discovered that matrix stiffening potently reduced the LGR5$^+$ ISC population. Additionally, the increased stiffness led to the expansion of OLFM4 from crypts to villus regions and promoted the differentiation of ISCs toward goblet cells. All these phenotypes were similarly observed in stiff colon samples from the murine colitis model and human patients with IBD.

YAP is a critical regulator of intestinal epithelial regeneration during inflammation[4] and tumorigenesis.[27,36] YAP activation can suppress WNT pathway and diminish LGR5$^+$ ISCs,[4,36] and can also promote the differentiation into Paneth cells[37] and goblet cells.[38] On the other hand, YAP activation induces a regenerative program via activating fetal marker genes (eg, expressing *Sca1* and *Anxa1*)[4] and epidermal growth factor receptor (EGFR) signaling.[27] We further demonstrated that YAP, as a downstream target of tissue stiffness, plays a critical role in the intestinal epithelial regeneration during IBD. Most notably, we comprehensively elucidated the divergent roles of cyto-YAP and nuc-YAP in determining the ISC differentiation trajectory. Matrix-stiffening–induced cyto-YAP expression drove the extension of OLFM4$^+$ cells into villus-like regions, whereas nuc-YAP expression led to a loss of LGR5$^+$ ISCs and increased differentiation toward goblet cells. The results of the scRNAseq analysis provided the stiffness-regulated transcriptional signatures of ISCs and their differentiated progeny, further corroborating the stiffness-dependent regulation of the ISC stemness and differentiation trajectory via YAP.

The metabolic pathway enrichment analysis as well as the direct assessment of glucose uptake and mitochondrial reactive oxygen species demonstrated that matrix stiffening augments ISC glucose demand and metabolism. Moreover, inhibiting glucose uptake on stiff matrix led to a shift toward soft matrix-like phenotype. These results are in-line with emerging evidence of the link between mechanical stimuli and energy metabolism.[39] Moreover, the activation of YAP could serve as a central core by sensing the mechanical stimuli to promote glucose metabolism.[40] In addition, it has been observed that intestinal tissues display elevated glucose metabolism in IBD.[41] Thus, the intestinal stiffening during IBD could mediate the fate of ISCs via YAP-induced metabolic rewiring. Therefore, exploiting the metabolic vulnerability of the mechano-stimulated ISCs could potentially offer a novel therapeutic strategy for IBD.

During the growth of the organoids, the cells in the crypt regions buckle the surface of the soft substrate, creating a curved invagination that mimics the in vivo crypt morphology. It is notable that the radius of the curvature in the crypt regions, even on the soft substrate, exceeds 250 μm. In comparison, the diameter of an ISC is in the order of 10 μm. Considering that a cell can sense a curvature when the curvature radius is in the same order of the cell size,[42] we do not anticipate considerable influence from the curvature in our system. Further investigations are warranted to determine how deeper curvatures influence the mechanobiology of ISCs and their communication with the Paneth cells that constitute their niche.

The potent impact of gut stiffening on OLFM4 expression and expansion may also have important implications in the context of IBD and colitis-associated colorectal adenocarcinoma (CAC). More specifically, although sporadic colorectal carcinoma is shown to be LGR5 positive,[43] most colitis-associated CACs lack LGR5 expression.[44] The mechanisms through which the 2 ISC markers, LGR5 and OLFM4, differently regulate CAC development remain to be determined. Here, in both the in vitro model and in the stiff human IBD colon, we observed that stiffening leads to an extension of OLFM4 into villus regions. This phenotype is reminiscent of our in vitro observations in which, on the stiff substrate, the OLFM4$^+$, LGR5$^-$ cells in the villus regions continuously gave rise to new crypts. This finding suggests that the OLFM4$^+$ cells in stiff colon are capable of generating new crypts, which could potentially lead to the development of CAC. Therefore, the signaling pathways involved in stiffening-induced OLFM4 extension might be potential clinical targets for colitis-associated CAC.

Supplementary Material

Note: To access the supplementary material accompanying this article, visit the online version of *Gastroenterology* at www.gastrojournal.org, and at https://doi.org/10.1053/j.gastro.2023.02.030.

References

1. Bloemendaal AL, Buchs NC, George BD, et al. Intestinal stem cells and intestinal homeostasis in health and in inflammation: a review. Surgery 2016;159:1237–1248.
2. Schmitt M, Schewe M, Sacchetti A, et al. Paneth cells respond to inflammation and contribute to tissue regeneration by acquiring stem-like features through SCF/c-Kit signaling. Cell Rep 2018;24:2312–2328.e7.
3. Wang Y, Chiang I-L, Ohara TE, et al. Long-term culture captures injury-repair cycles of colonic stem cells. Cell 2019;179:1144–1159.e15.
4. Yui S, Azzolin L, Maimets M, et al. YAP/TAZ-dependent reprogramming of colonic epithelium links ECM remodeling to tissue regeneration. Cell Stem Cell 2018;22:35–49.e7.
5. Stewart DC, Berrie D, Li J, et al. Quantitative assessment of intestinal stiffness and associations with fibrosis in human inflammatory bowel disease. PloS One 2018; 13(7):e0200377.

6. Johnson LA, Rodansky ES, Sauder KL, et al. Matrix stiffness corresponding to strictured bowel induces a fibrogenic response in human colonic fibroblasts. Inflamm Bowel Dis 2013;19:891–903.
7. He S, Azar DA, Esfahani FN, et al. Mechanoscopy: a novel device and procedure for in vivo detection of chronic colitis in mice. Inflamm Bowel Dis 2022;28:1143–1150.
8. Engler AJ, Sen S, Sweeney HL, et al. Matrix elasticity directs stem cell lineage specification. Cell 2006; 126:677–689.
9. Segel M, Neumann B, Hill MF, et al. Niche stiffness underlies the ageing of central nervous system progenitor cells. Nature 2019;573:130–134.
10. Mamidi A, Prawiro C, Seymour PA, et al. Mechanosignalling via integrins directs fate decisions of pancreatic progenitors. Nature 2018;564:114–118.
11. Altay G, Larrañaga E, Tosi S, et al. Self-organized intestinal epithelial monolayers in crypt and villus-like domains show effective barrier function. Scientif Rep 2019; 9:1–14.
12. Cruz-Acuña R, Quirós M, Farkas AE, et al. Synthetic hydrogels for human intestinal organoid generation and colonic wound repair. Nat Cell Biol 2017;19:1326–1335.
13. Gjorevski N, Sachs N, Manfrin A, et al. Designer matrices for intestinal stem cell and organoid culture. Nature 2016; 539:560–564.
14. Pérez-González C, Ceada G, Matejčić M, et al. Digesting the mechanobiology of the intestinal epithelium. Curr Opin Genet Develop 2022;72:82–90.
15. Barker N, Van Es JH, Kuipers J, et al. Identification of stem cells in small intestine and colon by marker gene Lgr5. Nature 2007;449:1003–1007.
16. Schlegelmilch K, Mohseni M, Kirak O, et al. Yap1 acts downstream of α-catenin to control epidermal proliferation. Cell 2011;144:782–795.
17. Pérez-González C, Ceada G, Greco F, et al. Mechanical compartmentalization of the intestinal organoid enables crypt folding and collective cell migration. Nat Cell Biol 2021;23:745–757.
18. Karam SM. Lineage commitment and maturation of epithelial cells in the gut. Front Biosci Landmark 1999; 4:286–298.
19. Snippert HJ, Van Der Flier LG, Sato T, et al. Intestinal crypt homeostasis results from neutral competition between symmetrically dividing Lgr5 stem cells. Cell 2010; 143:134–144.
20. VanDussen KL, Carulli AJ, Keeley TM, et al. Notch signaling modulates proliferation and differentiation of intestinal crypt base columnar stem cells. Development 2012;139:488–497.
21. Liu W, Li H, Hong S, et al. Olfactomedin 4 deletion induces colon adenocarcinoma in ApcMin/+ mice. Oncogene 2016;35:5237–5247.
22. Sato T, Van Es JH, Snippert HJ, et al. Paneth cells constitute the niche for Lgr5 stem cells in intestinal crypts. Nature 2011;469:415–418.
23. Dobrokhotov O, Samsonov M, Sokabe M, et al. Mechanoregulation and pathology of YAP/TAZ via Hippo and non-Hippo mechanisms. Clin Transl Med 2018; 7:1–14.
24. Wang C, Zhu X, Feng W, et al. Verteporfin inhibits YAP function through up-regulating 14-3-3σ sequestering YAP in the cytoplasm. Am J Cancer Res 2016;6:27.
25. Haber AL, Biton M, Rogel N, et al. A single-cell survey of the small intestinal epithelium. Nature 2017;551:333–339.
26. Wolf FA, Hamey FK, Plass M, et al. PAGA: graph abstraction reconciles clustering with trajectory inference through a topology preserving map of single cells. Genome Biol 2019;20:1–9.
27. Gregorieff A, Liu Y, Inanlou MR, et al. Yap-dependent reprogramming of Lgr5+ stem cells drives intestinal regeneration and cancer. Nature 2015;526:715–718.
28. Hong W, Guan K-L. The YAP and TAZ transcription co-activators: key downstream effectors of the mammalian Hippo pathway. Semin Cell Dev Biol 2012;23:785–793.
29. Sinner D, Kordich JJ, Spence JR, et al. Sox17 and Sox4 differentially regulate β-catenin/T-cell factor activity and proliferation of colon carcinoma cells. Mol Cell Biol 2007; 27:7802–7815.
30. Ohtsuka T, Ishibashi M, Gradwohl G, et al. Hes1 and Hes5 as notch effectors in mammalian neuronal differentiation. EMBO J 1999;18:2196–2207.
31. Jensen J, Pedersen EE, Galante P, et al. Control of endodermal endocrine development by Hes-1. Nat Genet 2000;24:36–44.
32. Schubert M, Klinger B, Klünemann M, et al. Perturbation-response genes reveal signaling footprints in cancer gene expression. Nat Commun 2018;9:1–11.
33. Wirtz S, Popp V, Kindermann M, et al. Chemically induced mouse models of acute and chronic intestinal inflammation. Nat Prot 2017;12:1295.
34. Smillie CS, Biton M, Ordovas-Montanes J, et al. Intra- and inter-cellular rewiring of the human colon during ulcerative colitis. Cell 2019;178:714–730.e22.
35. Gersemann M, Becker S, Nuding S, et al. Olfactomedin-4 is a glycoprotein secreted into mucus in active IBD. J Crohn's Colitis 2012;6:425–434.
36. Barry ER, Morikawa T, Butler BL, et al. Restriction of intestinal stem cell expansion and the regenerative response by YAP. Nature 2013;493:106–110.
37. Serra D, Mayr U, Boni A, et al. Self-organization and symmetry breaking in intestinal organoid development. Nature 2019;569:66–72.
38. Imajo M, Ebisuya M, Nishida E. Dual role of YAP and TAZ in renewal of the intestinal epithelium. Nat Cell Biol 2015; 17:7–19.
39. Evers TM, Holt LJ, Alberti S, et al. Reciprocal regulation of cellular mechanics and metabolism. Nat Metab 2021; 3:456–468.
40. Koo JH, Guan K-L. Interplay between YAP/TAZ and Metabolism. Cell Metab 2018;28:196–206.
41. Bhattaru A, Borja A, Zhang V, et al. FDG-PET/CT as the superior imaging modality for inflammatory bowel disease. J Nucl Med 2020;61:1159.
42. Assoian RK, Bade ND, Cameron CV, et al. Cellular sensing of micron-scale curvature: a frontier in understanding the microenvironment. Open Biol 2019;9:190155.
43. Hirsch D, Barker N, McNeil N, et al. LGR5 positivity defines stem-like cells in colorectal cancer. Carcinogenesis 2014;35:849–858.

44. Iwaya M, Ota H, Nakajima T, et al. Most colitis associated carcinomas lack expression of LGR5: a preliminary study with implications for unique pathways of carcinogenesis compared to sporadic colorectal carcinoma. BMC Cancer 2021;21:1–9.

Received April 27, 2022. Accepted February 17, 2023.

Correspondence
Address correspondence to: Nima Saeidi, PhD, Harvard Medical School, 51 Blossom Street, Room 206, Boston, Massachusetts 02114. e-mail: nsaeidi@mgh.harvard.edu.

Acknowledgments
The authors thank Dr. Ramnik J. Xavier, the Director of the Center for the Study of Inflammatory Bowel Disease at Massachusetts General Hospital (National Institutes of Health, P30DK043351) for his constructive comments, providing human samples, and sharing the human scRNAseq data. The authors thank Maris A. Handley and Jacqueline Choi from the HSCI-CRM Flow Cytometry Core and iHisto Inc. for their support. The authors also thank Ann S. Adams for editorial advice.

CRediT Authorship Contributions
Shijie He, PhD (Conceptualization: Lead; Data curation: Lead; Formal analysis: Lead; Investigation: Lead; Methodology: Lead; Resources: Lead; Software: Lead; Supervision: Supporting; Validation: Lead; Visualization: Lead; Writing – original draft: Lead; Writing – review & editing: Lead).

Peng Lei, PhD (Investigation: Equal; Methodology: Equal; Validation: Equal; Visualization: Equal).

Wenying Kang, PhD (Methodology: Equal; Software: Equal; Validation: Supporting).

Priscilla Cheung, PhD (Methodology: Equal; Resources: Supporting; Validation: Supporting; Visualization: Supporting).

Tao Xu, PhD (Methodology: Supporting; Validation: Supporting; Visualization: Supporting).

Miyeko Mana, PhD (Methodology: Supporting; Validation: Supporting; Visualization: Supporting; Writing – review & editing: Supporting).

Chan Young Park, PhD (Methodology: Supporting).

Hongyan Wang, MD (Investigation: Supporting; Methodology: Supporting).

Shinya Imada, PhD (Methodology: Supporting).

Jacquelyn O. Russell, PhD (Methodology: Supporting).

Jianxun Wang, PhD (Investigation: Supporting; Methodology: Equal).

Ruizhi Wang, PhD (Methodology: Equal).

Ziheng Zhou, MD (Methodology: Supporting).

Kashish Chetal, PhD (Methodology: Supporting; Software: Supporting).

Eric Stas, PhD (Methodology: Supporting).

Vidisha Mohad, PhD (Methodology: Equal).

Peter Bruun-Rasmussen, PhD (Methodology: Supporting).

Ruslan I. Sadreyev, PhD (Methodology: Supporting; Resources: Supporting; Supervision: Supporting).

Richard A. Hodin, MD (Methodology: Supporting; Supervision: Supporting; Writing – review & editing: Supporting).

Yanhang Zhang, PhD (Methodology: Supporting; Supervision: Supporting).

David T. Breault, PhD (Methodology: Supporting; Supervision: Supporting).

Ömer H. Yilmaz, MD (Methodology: Supporting; Resources: Supporting; Supervision: Supporting).

Fernando D. Camargo, MD (Methodology: Supporting; Resources: Supporting; Supervision: Supporting).

Jeffrey J. Fredberg, PhD (Methodology: Supporting; Resources: Supporting; Supervision: Supporting).

Nima Saeidi, PhD (Conceptualization: Supporting; Funding acquisition: Lead; Methodology: Supporting; Supervision: Lead; Writing – original draft: Supporting; Writing – review & editing: Supporting).

Conflicts of interest
The authors disclose no conflicts. N.S. and S.H. are inventors on a patent application filed based on this investigation.

Funding
This work was supported by funding from the National Institutes of Health (R01DK123219 and K01DK103947 to N.S., and R01HL148152 and U01CA202123 to J.J.F.), Executive Committee on Research/Massachusetts General Hospital (2019A002949 to N.S.), and Polsky Family Fund (to N.S.).

Data Availability
The processed sc-RNA-seq data of the mouse organoids are provided in the Supplementary Table. All material and data requests should be submitted to the corresponding author for consideration.

Supplementary Materials and Detailed Methods

Fabrication of Hydrogel Matrix

Polyacrylamide (PA) hydrogel matrices were fabricated on 35-mm glass bottom dishes (Cellvis, D35-20-1.5-N) as described.[1] To determine which extracellular matrix (ECM) protein most efficiently supported cell growth, we tested hydrogels coated with collagen I (Advanced Biomatrix, 5005), laminin (Sigma, L2020-1mg), collagen IV (Advanced Biomatrix, 5022), and fibronectin (Advanced Biomatrix, 5050; Sigma, F1141). Collagen I was determined to be the best protein for cell spreading and long-term growth, followed by laminin. Collagen IV could only support a few small colonies (Supplementary Figure 10*A*). Fibronectin barely supported any growth at all. Similar to the collagen-I–coated hydrogel, increasing the stiffness of the laminin-coated hydrogels diminished crypt size and promoted MUC2^{+} goblet cell differentiation (Supplementary Figure 10*B*). The recipes for preparing the matrices in accordance with the Young's modulus formula were: 3% acrylamide (Bio-Rad, 1610140) and 0.058% bisacrylamide (Bio-Rad, 1610142) for 0.6 kPa; 7.5% acrylamide and 0.034% bisacrylamide for 2.4 kPa; and 7.5% acrylamide and 0.148% bisacrylamide for 9.6 kPa. The Young's modulus of the gel was measured using Asylum MFP-3D atomic force microscopy microindentation and calculated from the fitting force-indentation data using a Hertz sphere model (Supplementary Figure 10*C*).[2] Uniform collagen-I coating on the gel surface was confirmed via immunofluorescent staining (Supplementary Figure 10*D*).

ERN Media Recipe and Antibodies for Immunofluorescence, Immunohistochemistry, and Flow Cytometry

ENR media was advanced DMEM/F12 (Gibco, 12634-028) supplemented with 50 ng/mL epidermal growth factor (EGF) (Peprotech, 315-09), 100 ng/mL Noggin (Peprotech, 250-38), 10% R-spondin conditional media (iLab in Harvard digestive center), 1% Glutamax (Gibco, 35050-061), 1% HEPES (Gibco, 15630-080), 0.2% Primocin (Invitrogen, ant-pm-2), 0.2% Normocin (Invitrogen, ant-nr-2), 1% B27 (Gibco, 12587010), 0.5% N2 (Gibco, 17502-048), and 1.25 mmol/L N-Acetyl-Cystein (Sigma, A8199). Rabbit primary antibodies were used for staining villin (ab130751), MUC2 (ab76774, ab272692), CHRO-A (ab15160), LYZ (ab2408), non-phosphorylated YAP (ab205270), TFF3 (ab272927), KI-67 (cs9129), OLFM4 (ab105861, cs14369), Ser127 Phospho-YAP (cs13008), Glut2 (PA5-77459, Thermo Fisher Scientific), COLLAGEN I (ab34710), and COLLAGEN IV (ab6586). Mouse primary antibodies were used for total YAP (ab56701) and VILLIN (Proteintech, 66096-1-Ig). Goat anti-rabbit/mouse Alexa Fluor 405, 488, 594 and 647 (Thermo Fisher) were used as secondary antibodies. DAPI (Fisher scientific, D1306) and UEA-I Fluorescein (Vector labs, FL-1061-5) were used for staining nuclei and Paneth cells, respectively. To make the antibody cocktail of flow cytometry, SMEM (Sigma, M8167) was supplemented with CD45-PE (1:500, eBioscience, 30-F11), CD31-PE (1:500, Biolegend, Mec13.3), Ter119-PE (1:500, Biolegend, Ter119), CD24-Pacific Blue (1:300, Biolegend, M1/69), EPCAM-APC (1:300, eBioscience, G8.8), and CD117(C-kit)-APC-CY7 (1:300, Thermo fisher, 47-1171-80). After staining, 10 mL SMEM was added and the samples were centrifuged for 5 minutes at 300*g*. The pellets were resuspended with 1 mL SMEM supplemented by 7-AAD (1:500, Thermo Fisher A1310) and filtered through a 40-μm mesh (BD Falcon) before cell sorting with a BD FACS Aria II cell sorter. ISCs were isolated as LGR5-EGFP^{high}EPCAM^{+} CD24$^{low/-}$ CD31^{-} TER119^{-} CD45^{-} and 7-AAD^{-}, TA progenitors were isolated as LGR5-EGFP^{low} EPCAM^{+} CD24 $^{low/-}$ CD31^{-} TER119^{-} CD45^{-} and 7-AAD^{-}, and Paneth cells were isolated as CD24^{high} Sidescatter^{high} C-KIT^{+} LGR5-EGFP^{-} EPCAM^{+} CD31^{-} TER119^{-} CD45^{-} and 7-AAD^{-}.

Immunofluorescence, Immunohistochemistry, and In Situ Hybridization

For in vitro immunofluorescence (IF), cells were fixed in 4% paraformaldehyde/phosphate-buffered saline (PBS) for 10 minutes and cold 70% ethanol for 30 minutes, permeabilized in 0.3% Triton X-100/PBS for 20 minutes, and blocked in 2% bovine serum albumin for 30 minutes. The cell layers were stained with primary antibody, then stained with secondary antibodies. Laser scanning microscopy images were captured by using the inverted confocal microscope (Nikon C2, 20X or 60X objective). The average intensity of the fluorescent signals in these images was then quantified using a custom-made MATLAB code that identifies crypt-like regions based on the density of the nuclei (Supplementary Figure 9*E* and *F*). All the fluorescent images represented at least 9 field views from 3 different animals (3 field views/animal). Histologic samples were processed, embedded in paraffin, and sectioned at 4 μm. Paraffin sections were then deparaffinized and hydrated. Antigen retrieval was achieved by boiling the sections in 10 mmol/L sodium citrate. Sections were then washed with PBS 3 times, treated with 3% H_2O_2 for 15 minutes, and thereafter with 5% bovine serum albumin for 20 minutes. The sections were incubated with primary antibodies overnight at 4°C. Subsequently, the sections were immunohistochemically stained with secondary antibodies for 50 minutes at room temperature. All the human samples were deidentified. Single-molecule in situ hybridization was performed using Advanced Cell Diagnostics (ACD) RNAscope 2.0 HD Detection Kit (Fast Red dye) for the probes of LGR5 (ACD, 311021) and OLFM4 (ACD, 311041). For flow cytometry, cold SMEM (1:5) was added to stop the trypsinization after collecting the cells, followed by centrifuging for 5 minutes at 300*g*. The cell pellets were resuspended and stained for 15 minutes on ice in 1 mL antibody cocktail. More details for recipe of ENR media, antibodies, colon stiffness measurement, and single-cell RNA sequencing are provided in Supplementary Materials.

Uniaxial Tensile Testing for Colon Stiffness Measurement

The colons collected from the chronic colitis experiments were cut open in the longitudinal direction into flat

rectangular patches using a surgical scalpel. Sandpaper tabs were glued to both ends of the sample to prevent slippage during testing. The effective length (l_0, ie, sandpaper-to-sandpaper distance) and width (w) of each sample was measured using a caliper. The cross-section view of the colon supported with a 10 μL tip was imaged, and the thickness (t) of the section was measured using Image-J. Samples were mounted on an Instron uniaxial tester (Instron, Norwood, MA) by clamping the sandpaper tabs with the grips attached to the tester (Supplementary Figure 9*G* and *H*). Samples were moisturized with PBS spray before each test was started. Steady-state uniaxial tensile tests were performed by fixing one end of the sample and pulling away the other end with an extension rate of 0.02 mm/s. The pulling force (F) and the displacement (d) of the moving end of the sample were recorded at a frequency of 5 Hz. The end of the regime of elastic deformation was marked by a drop in the slope of the force-displacement curve. The strain (ε) of the sample was obtained as

$$\varepsilon = \frac{d}{l_0}.$$

Assuming tissue incompressibility, the Cauchy stress (σ) can be calculated as

$$\sigma = \frac{F}{wt}(1+\varepsilon).$$

Culture of 3D Organoids in Matrigel Transferred From the 2D Hydrogel

The cells on the hydrogel matrix were trypsinized using TrypLE for 5 minutes at 37°C. The wells were sealed with a lid and the bottom of the well tray was vigorously slammed on the table to detach the cells. After collecting the cells/clusters, cold SMEM (1:5) was added to stop the trypsinization, followed by centrifuging for 5 minutes at 300*g*. The cell pellets were resuspended in ENR media and Matrigel (1:1, Corning 356231), and then 25 μL/well was seeded in 48-well plates and stored at 37°C for solidification. After 20 minutes, 300 μL/well ENR media was added and thereafter changed every 3 days. The 3D organoids were imaged on day 5.

scRNAseq of Gut Organoids

Sample preparation and quality control. The organoids grown on the soft vs stiff substrates were digested into single cells and collected as 2 separated groups (soft vs stiff) to perform the scRNAseq analysis. This experiment was performed with biological triplicate samples (Supplementary Figure 7*A*). For the sake of quality control, cells with <200 expressed genes and genes expressed in <3 cells were filtered out. Then, we excluded the cells with mitochondrial transcripts >20% and unique feature counts >6000 or <200. After filtering 4200–5000 high-quality cells for each sample were included in the analysis. Counts across all cells for each sample were normalized using NormalizeData function and the effect of the cell cycle was removed by regressing the difference out between the S phase and G2M phase from normalized data. As shown in Supplementary Figure 11, we verified that regressing out the cell cycle genes allows for the identification of unique clusters for ISCs and TA cells.

ScRNAseq Library Construction

The scRNAseq library was constructed on the Chromium 10x instrument using Chromium single cell 3' reagent v3.0 kits, followed by sequencing on Illumina HiSeq 2500 instruments, which resulted in approximately 160 million reads per sample. Initial processing of scRNAseq data was performed using CellRanger (v4.0.0)

(https://support.10xgenomics.com/single-cell-gene-expression/software/overview/welcome). In brief, reads were aligned to the mm10 mouse reference genome with the mapping rate of ~70%, followed by the generation of read counts per gene in each cell. Further analysis was performed using the Seurat 3.2.3 package (https://satijalab.org/seurat/).

Cell Clustering and Differential Expression Analysis

Using the FindVariableFeatures function, we selected 2000 features to be used in a Principal Component Analysis. UMAP dimensionality reduction and cell clustering were performed using RunUMAP and FindClusters functions, respectively. VlnPlot and FeaturePlot functions were used to generate violin plots and feature plots for the datasets. Heatmaps of gene expression were generated using DoHeatmap function. To identify specific cell populations via a uniform and fair clustering process for all the samples and ensure sufficient cell number for rare cell populations, such as, tuft cells and EECs, cells from all samples were integrated using Seurat canonical correlation analysis method. Integration anchors were obtained using the FindIntegrationAnchors function. IntegrateData function was used to integrate individual datasets. The FindMarkers function was applied to the integrated samples to identify differentially expressed genes between the cell subsets. Biological annotation of cell clusters was based on the expression of known cell type markers. The analysis of differential gene expression was performed on each individual normalized sample without sample integration (3 samples from soft substrate and 3 samples from stiff substrate) to identify the gene expressions significantly impacted by stiffness.

PROGENy Analysis

The PROGENy tool was used to analyze the 14 different pathways including WNT, EGFR, transforming growth factor beta (TGF-β), P53, and so on, according to the method described in https://saezlab.github.io/progeny/articles/progeny.html. A model matrix based on top 500 differential expressed genes of soft vs stiff substrates was created to compute the PROGENy activity scores (Supplementary Figure 7*F*).

scProportionTest for the Ratio Analysis of Soft vs Stiff Substrate

To analyze the changes of proportions of each cell type on soft vs stiff substrate, we used a standard tool scProportionTest (https://github.com/rpolicastro/scProportionTest) that is based on random bootstrapping simulation to assess statistical significance of differences between cell proportions in scRNAseq samples. Using scProportionTest, we compared the proportions of each cell type between the soft substrate and the stiff substrate (Figure 5*C*). Statistical significance was assessed based on the cutoffs of the false discovery rate (FDR)-adjusted $P < 0.05$.

scRNAseq Analysis for Human Colon Epithelium

Cell clustering and differential expression analysis. We reanalyzed scRNAseq data from the colon biopsy specimen generated by Smillie et al[3] (raw data from https://portals.broadinstitute.org/single_cell/study/SCP259). Samples from both male and female patients were included in the analysis. From the dataset, we used epithelial samples containing healthy tissue samples as well as inflamed tissue samples from patients with UC. We followed the same procedure to identify cell clusters as outlined in Smillie et al,[3] using Seurat (https://satijalab.org/seurat/, v.3.2.3) and Phenograph. The only exception was we used a larger k = 1000 when applying Phenograph to KNN-graphs and then reclustered with k = 50 to identify rare epithelial cell types. Cell clusters were identified by gene expression with known cell type markers. Barnes-Hut t-Distributed Neighbor Embedding on PCS (perplexity = 10; iterations = 5000) provided visualization of data embedding. The coarser k resulted in larger cell clusters where immature forms of cell types are no longer differentiated from the terminally differentiated cell types. The MAST model is suitable for identifying cell type markers and differential expression genes in inflamed tissue samples with control tissue. The discrete coefficient of MAST model output is reported in the text and figures unless otherwise stated.

Identifying Statistically Significant Differences in Cell Proportions

Samples with exceedingly small numbers of cells yielded few cell types and disproportionate cell type proportions. Therefore, we excluded samples containing <250 cells from subsequent analysis. Changes in cell proportions between healthy and inflamed tissues were assessed by 2 methods. First, we performed a Monte Carlo test, where H0 is the difference in the proportions of each cell type (inflamed vs healthy condition) as a consequence of random sampling. To conduct this test, we combined cells from both conditions and then randomly segregated the cells back into the 2 conditions while maintaining the original sample sizes, repeating the process 1000 times. Then we recalculated the proportional difference between the 2 conditions and compared this value to the observed proportional difference for each cell type. The *P* value reflects the number of simulations wherein the simulated proportional difference was more than that observed. This test reflects how enriched each cell type is within each condition (healthy or inflamed), but it does not account for the specimen from which each cell was isolated. In the second method, we calculated the relative variation in each cell type proportion between all pairs of healthy donors as a control. Then we calculated the relative variation in each cell type by dividing the fraction of the cell type in each inflamed specimen by that of a healthy specimen. After $\log_2$ transformation, we conducted a 2-sided Kolmogorov-Smirnov test of the relative variation in composition between the control (healthy) and inflamed groups (Kolmogorov-Smirnov test function).

Identifying Significant Changes in Pathway Gene Signatures

The ECM pathway (YAP1ECM_AXIS) was obtained from WikiPathways and the WNT signaling pathway was obtained from KEGG. Pathway enrichment analysis was performed using gene sets from these pathways and the fgsea package in R. The shared genes between significant cell types were used as gene signatures for the pathways of interest. The expression of each gene was then scaled by its root mean squared expression across all cells, and the mean scaled expression for all signature genes in the pathway was calculated to give a signature score for each cell. We then used mixed linear models to identify changes in expression levels of gene signatures in the inflamed state. In the model, the fixed effect term is used to represent the condition of each cell (healthy or inflamed) and the random intercept that varies with each sample is used to account for the sample from which each cell was isolated. Analysis of variance is used to estimate the fixed term *P* value.

Supplementary References

1. He S, Carman CV, Lee JH, et al. The tumor suppressor p53 can promote collective cellular migration. PloS One 2019;14:e0202065.
2. Mih JD, Sharif AS, Liu F, et al. A multiwell platform for studying stiffness-dependent cell biology. PloS One 2011;6:e19929.
3. Smillie CS, Biton M, Ordovas-Montanes J, et al. Intra- and inter-cellular rewiring of the human colon during ulcerative colitis. Cell 2019;178:714–730.e22.

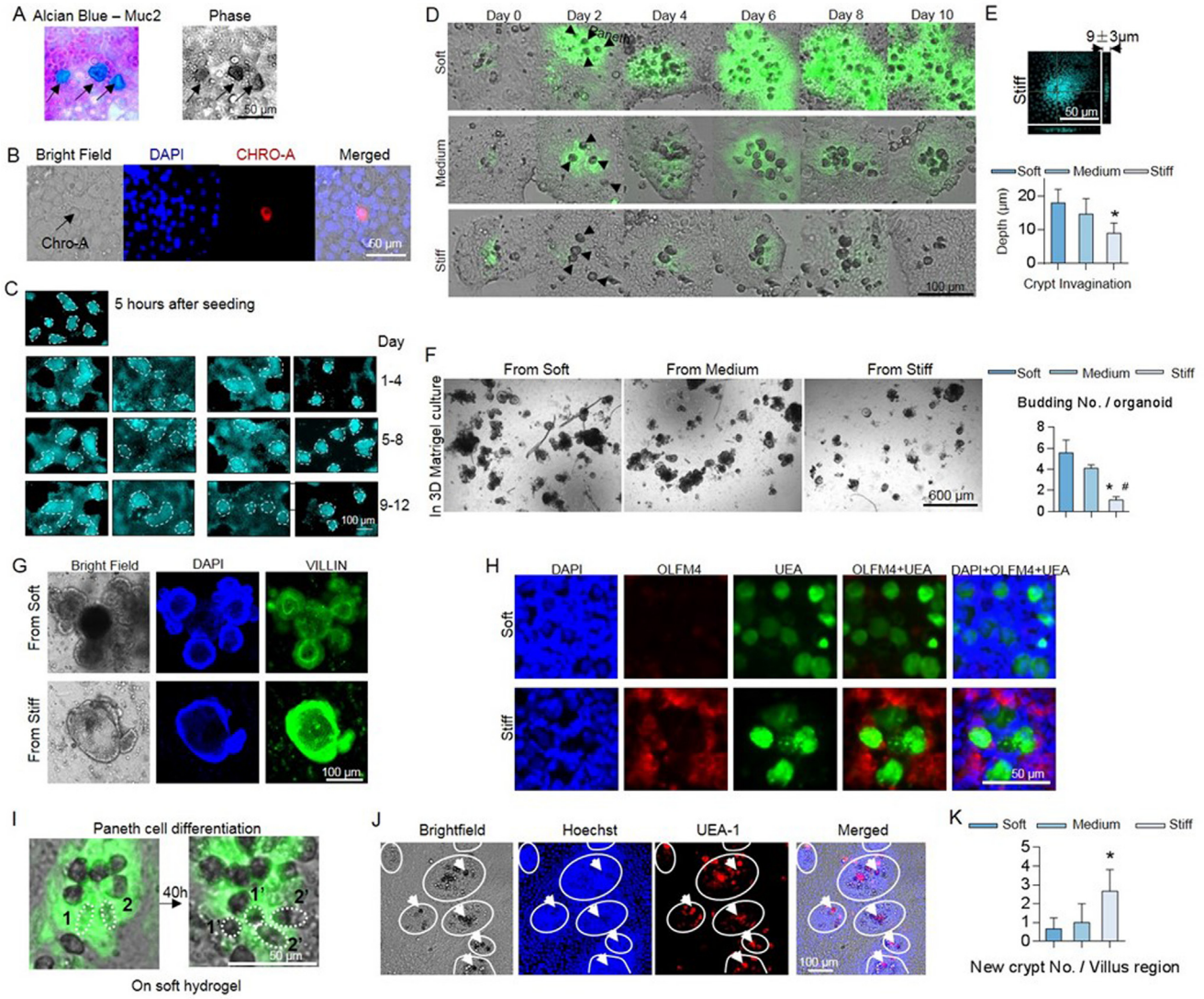

Supplementary Figure 1. (*A*) AB staining for Muc2 confirmed the presence of mature goblet cells in the organoids, which were also distinguishable in the phase image from the surrounding cells due to the different contrast of high-content muc2 glycoprotein. Scale bar, 50 μm. (*B*) CHRO-A$^+$ EECs were present in the villus-like regions. Scale bar, 50 μm. (*C*) Daily DAPI staining from 5 h after seeding to Day 12 showed that the villus-like regions exhibited a turnover rate of 3–4 d (n = 5). The *white contour lines* indicate the crypt regions. Scale bar, 100 μm. (*D*) Long-term live-cell imaging exhibited a completely different phenotype of LGR5-EGFP$^+$ ISCs between the soft matrix and the stiff matrix. More specifically, on the soft matrix, the LGR5-EGFP$^+$ ISCs continuously increased and expanded throughout the culture period. In contrast, LGR5-EGFP$^+$ ISCs on the stiff matrix progressively diminished over time, nearly disappearing by the 10th day. The medium matrix was able to maintain some LGR5-EGFP$^+$ ISCs. Scale bar, 100 μm. (*E*) Orthogonal projection showing buckling of the hydrogel surface. Increasing the hydrogel stiffness significantly inhibited crypt invagination ($P < 0.05$; n = 3). "Soft" is for 0.6 kPa, and "Stiff" is for 9.6 kPa. Scale bar, 50 μm. (*F*) The 3D organoids from the soft or medium matrix budded, but those from the stiff matrix grew as cysts with less budding (n = 3). Scale bar, 600 μm. (*G*) Villin expression in the organoids generated from the cells that were pre-conditioned on stiff gels was greater than that generated from the soft gels (n = 3). Scale bar, 100 μm. (*H*) In the interior of the crypt-like regions, OLFM4$^+$ cells were located adjacent to UEA$^+$ Paneth cells on the stiff matrix (n = 3). Scale bar, 50 μm. (*I*) LGR5-EGFP$^+$ ISCs (1 and 2) differentiated into 2 Paneth cells (1' and 2') on the soft matrix (Video 1; n = 3). Scale bar, 50 μm. (*J*) The bright-field image from living cell imaging was counterstained with Hoechst 33342 for nuclei and UEA for secretory cells. The superimposed image showed that the UEA$^+$ Paneth cells, which are located in the crypt regions, are large and optically dark. Furthermore, the nuclear staining showed that the cells in crypt regions were more densely packed compared with the surrounding villus regions. The *white contour lines* and the *arrows* denote the crypt regions and the Paneth cells, respectively. UEA$^+$ cells in the villus regions could be other secretory cells, such as goblet cells. Scale bar, 100 μm. (*K*) There was more new crypt generation in the villus-like regions on the stiff matrix than on the soft matrix (Video 2 for soft matrix and Video 3 for stiff matrix; n = 3). *Vs soft and #vs medium; $P < 0.05$ (1-way analysis of variance [ANOVA]).

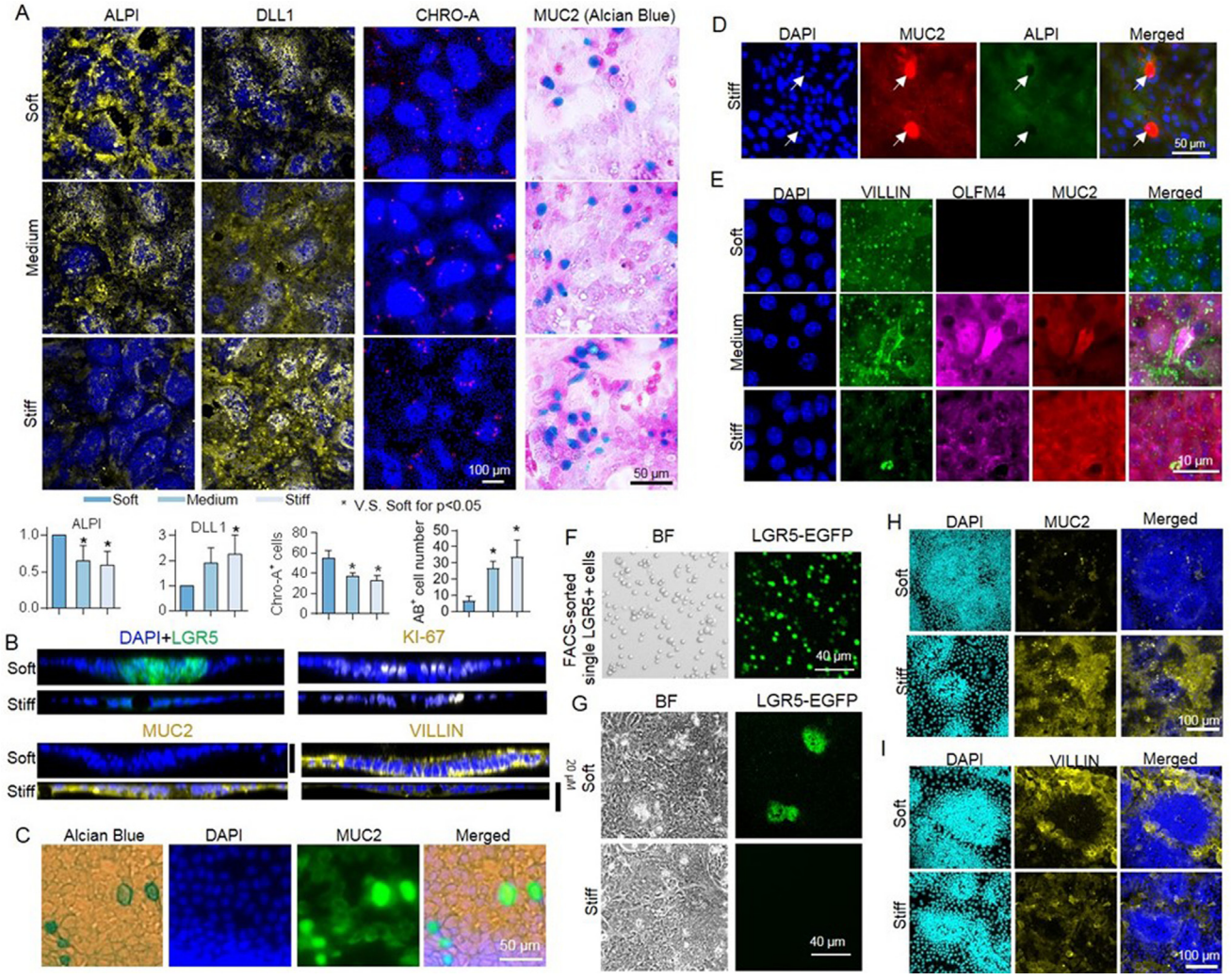

Supplementary Figure 2. (*A*) Stiffening decreased the expression of ALPI and CHRO-A, and increased the expression of DLL1 and mature AB-positive goblet cells in the villus regions (n = 3). ALPI and DLL1 were quantified via their fluorescent intensity. The number of CHRO-A^{+} and AB+ cells were counted per field of view. (*B*) The side views of the expression of LGR5, KI-67, MUC2, and VILLIN for both the soft substrate and the stiff substrate. Scale bar, 20 μm. (*C*) Costaining of MUC2 and AB showed that MUC2^{hi} cells were AB^{+} mature goblet cells. The pink color of AB staining in Supplementary Figure 1 was faded in purpose via immersing in water overnight to avoid interference with the fluorescent channels of DAPI and MUC2. Scale bar, 50 μm. (*D*) On the stiff substrate, the cells with strong MUC2 expression did not express the enterocyte marker, ALPI. The cells with weak MUC2 expression simultaneously expressed ALPI. Scale bar, 50 μm. (*E*) On the soft gels, the cells in the villus region only expressed VILLIN. On the medium gels, the cells co-expressed VILLIN, OLFM4, and weak MUC2. On the stiff gels, the cells coexpressed MUC2, OLFM4, and weak VILLIN (n = 3). Scale bar, 10 μm. (*F*) Flow cytometry-sorted single LGR5^{+} ISCs were seeded on the gels. Scale bar, 40 μm. (*G*) The single ISCs assembled automatically, forming crypt-villus structures. The LGR5^{+} crypts were visible on the soft gels. Scale bar, 40 μm. As with the intact crypt seeding, increased gel stiffness promoted MUC2 expression (*H*) and suppressed VILLIN expression (*I*). Scale bars in (*H*) and (*I*), 100 μm. *Vs soft and # vs medium; $P < 0.05$ (one-way analysis of variance).

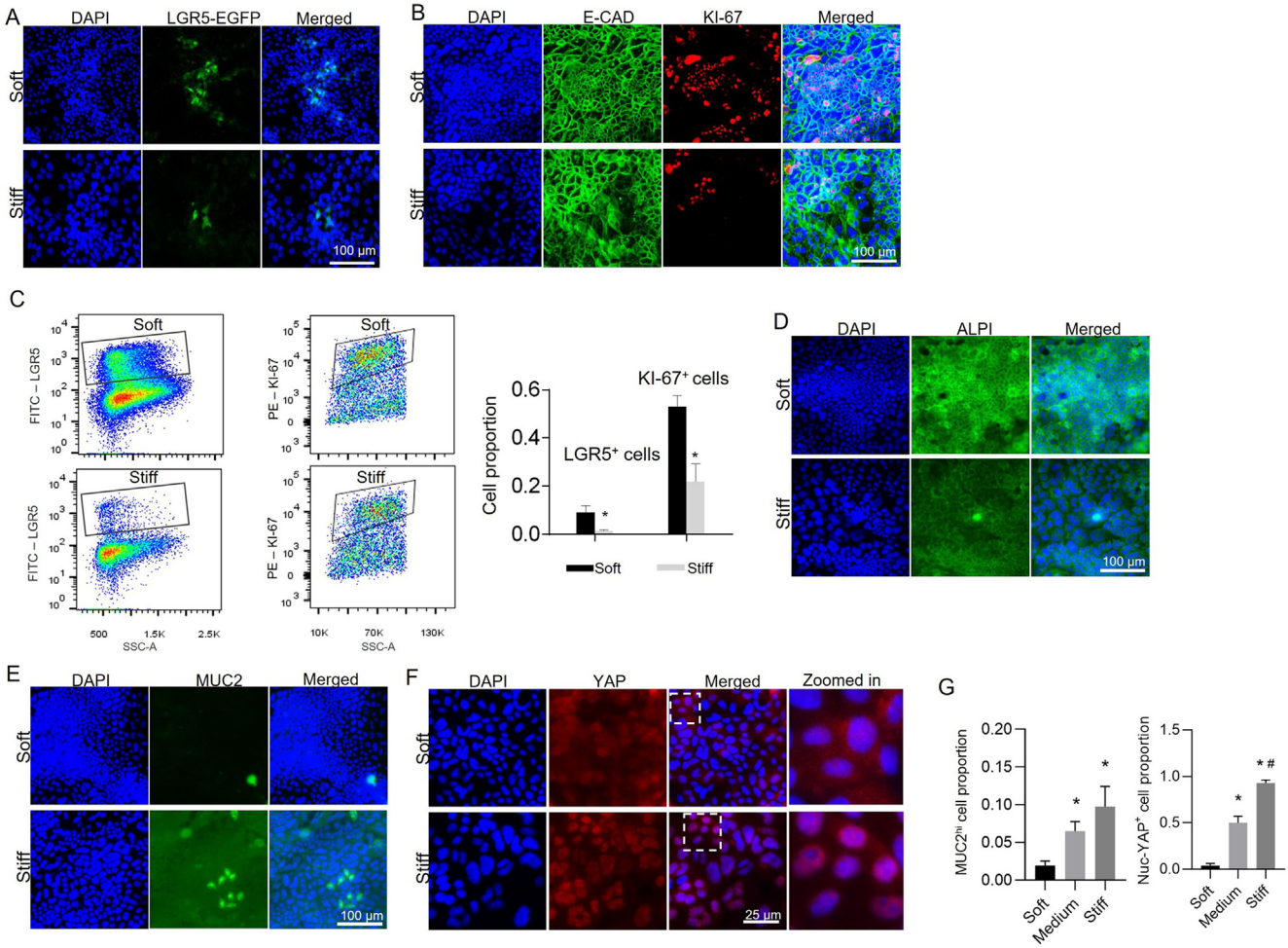

Supplementary Figure 3. (*A*) Stiff substrate diminished LGR5^{+} colon stem cells (*A*) and KI-67^{+}–proliferating cells (*B*), as confirmed using flow cytometry (*C*). The continuous expression of E-cadherin confirmed the epithelial cell type (*B*). Stiff substrate suppressed the expression of the enterocyte marker, ALPI (*D*), and increased the goblet cell marker, MUC2 (*E*). Also, increasing stiffness promoted the YAP nuclear translocation that drove the goblet cell differentiation (*F*). n = 3. Scale bar, 100 μm in *A–D* and 25 μm in *E*. The proportions of cells with high MUC2 expression and nuc-YAP^{+} cells were quantified in *G*.

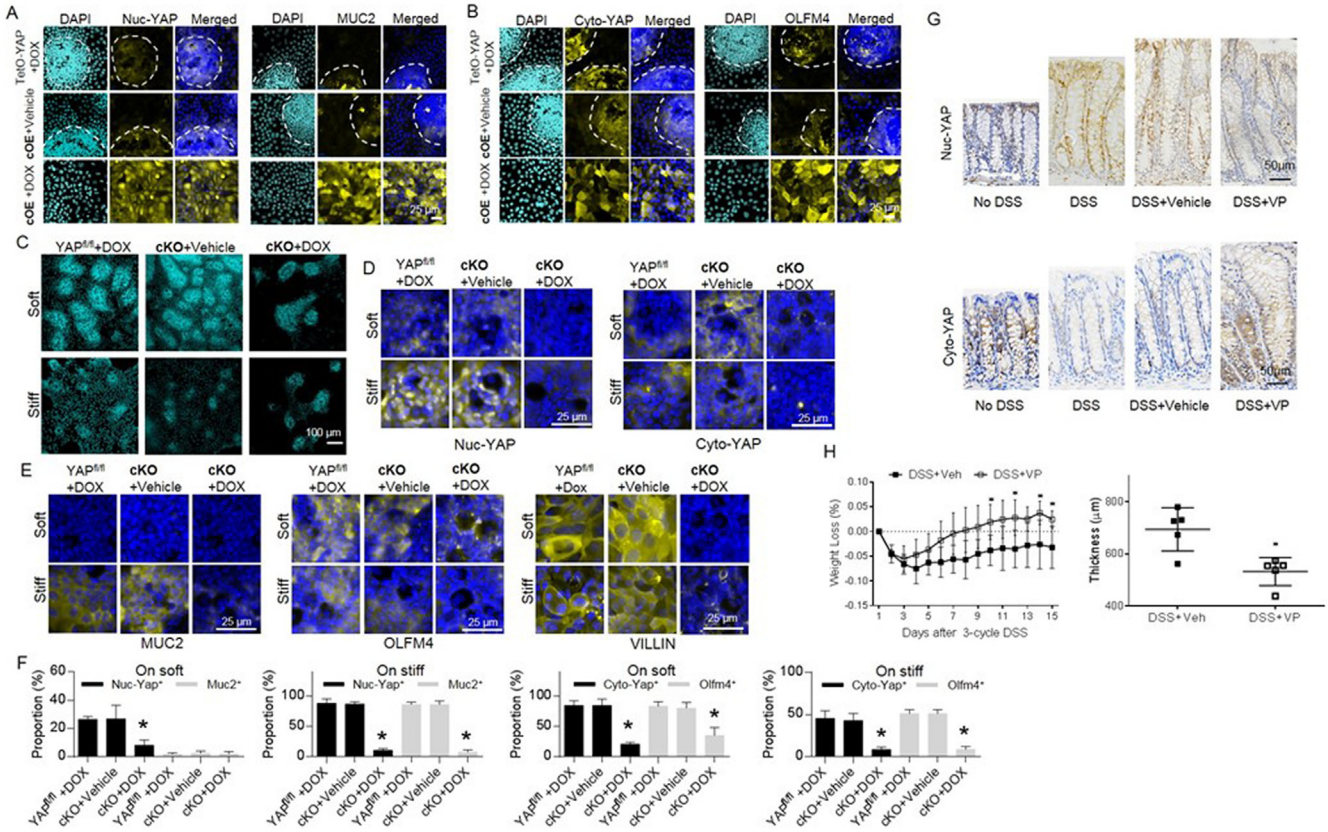

Supplementary Figure 4. Staining for YAP cOE cells + DOX and the control groups, tetO-YAP cells + DOX and YAP cOE cells + vehicle (deionized water) showed that increasing the expression of nuc-YAP (*A*) and cyto-YAP (*B*) by cOE promoted MUC2 and OLFM4, respectively. The *white dashed lines* trace the crypt-like regions. n = 3. Scale bars in *A* and *B*, 25 μm. (*C*) The villus-like regions vanished from the YAP cKO cells. $YAP^{fl/fl}$ cells with DOX and YAP cKO cells with vehicle served as control groups. Scale bar, 100 μm. (*D* and *E*) The leftover crypt-like regions were enriched with Paneth cells and were negative for nuc-YAP and MUC2, as well as cyto-YAP, OLFM4, and VILLIN. The control groups comprised YAP cKO cells administered with vehicle and $Yap^{fl/fl}$ cells treated with DOX and showed the distinct crypt-villus regions we observed previously. n = 3. Scale bar, 25 μm. (*F*) Quantification of *D* and *E* shows the impacts of YAP KO on the proportions of nuc-YAP^{+} cells and $MUC2^{+}$ cells, and cyto-YAP^{+} cells and $OLFM4^{+}$ cells in total cells. Compared with the control groups, ie, $Yap^{fl/fl}$+DOX and cKO+Vehicle, loss of nuc-YAP and cyto-YAP expressions, respectively, lead to the reduction of $MUC2^{+}$ cells and $OLFM4^{+}$ cells. (*G*) Immunohistochemistry staining of nuc-YAP and cyto-YAP throughout the entire bottom-to-top structure of the colon epithelium. The DSS-induced colitis was associated with increased nuc-YAP expression, and VP administration in the DSS-induced colitis mice suppressed nuc-YAP expression and increased the expression of cyto-YAP. Scale bar, 50 μm. (*H*) VP administration mitigated the body weight loss and colon thickening of the DSS-induced colitis mice. n = 5. $^{*}P < 0.05$ (1-way ANOVA in *F* and Student *t* test in *H*).

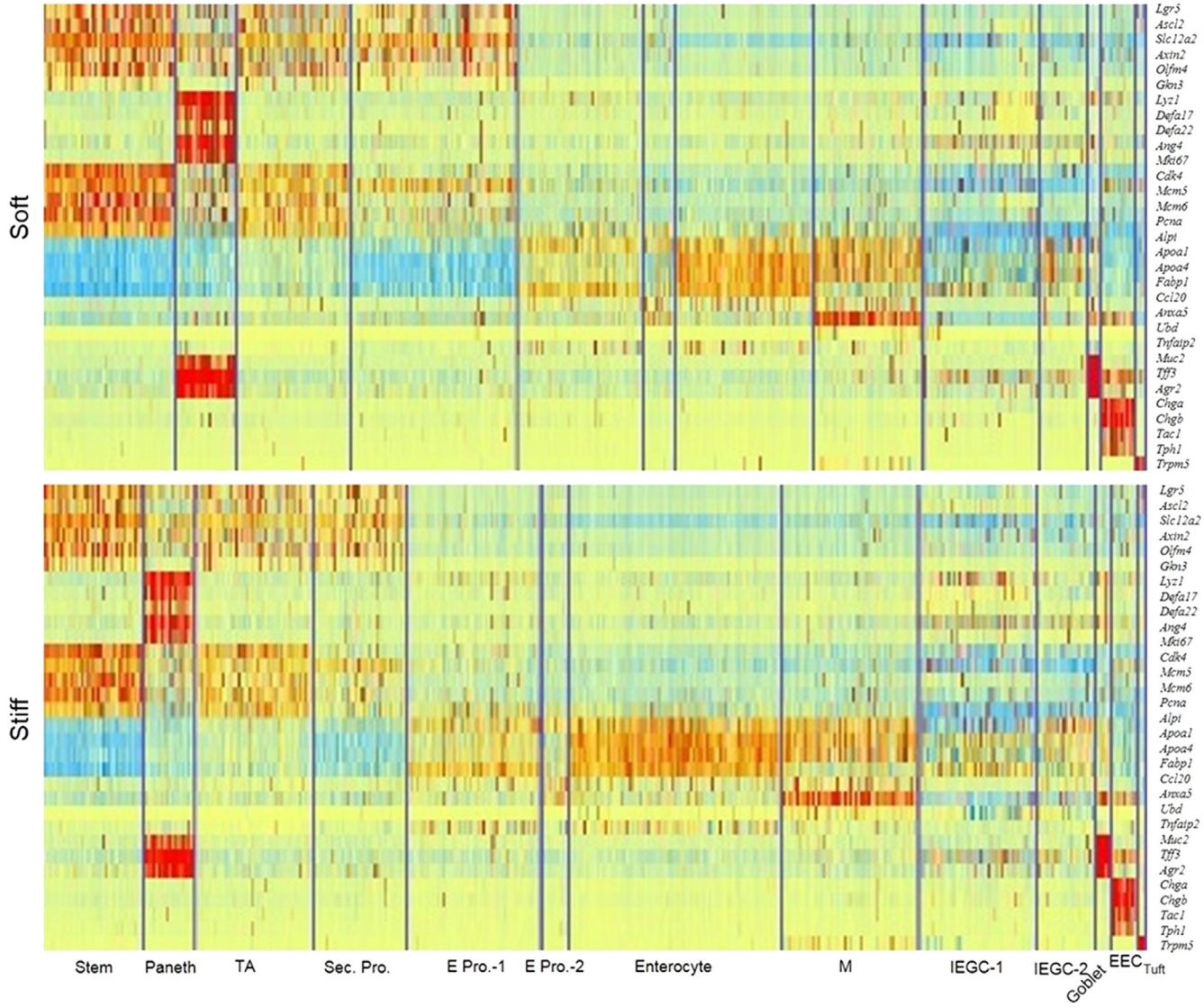

Supplementary Figure 5. Full labels of marker genes for each cell type.

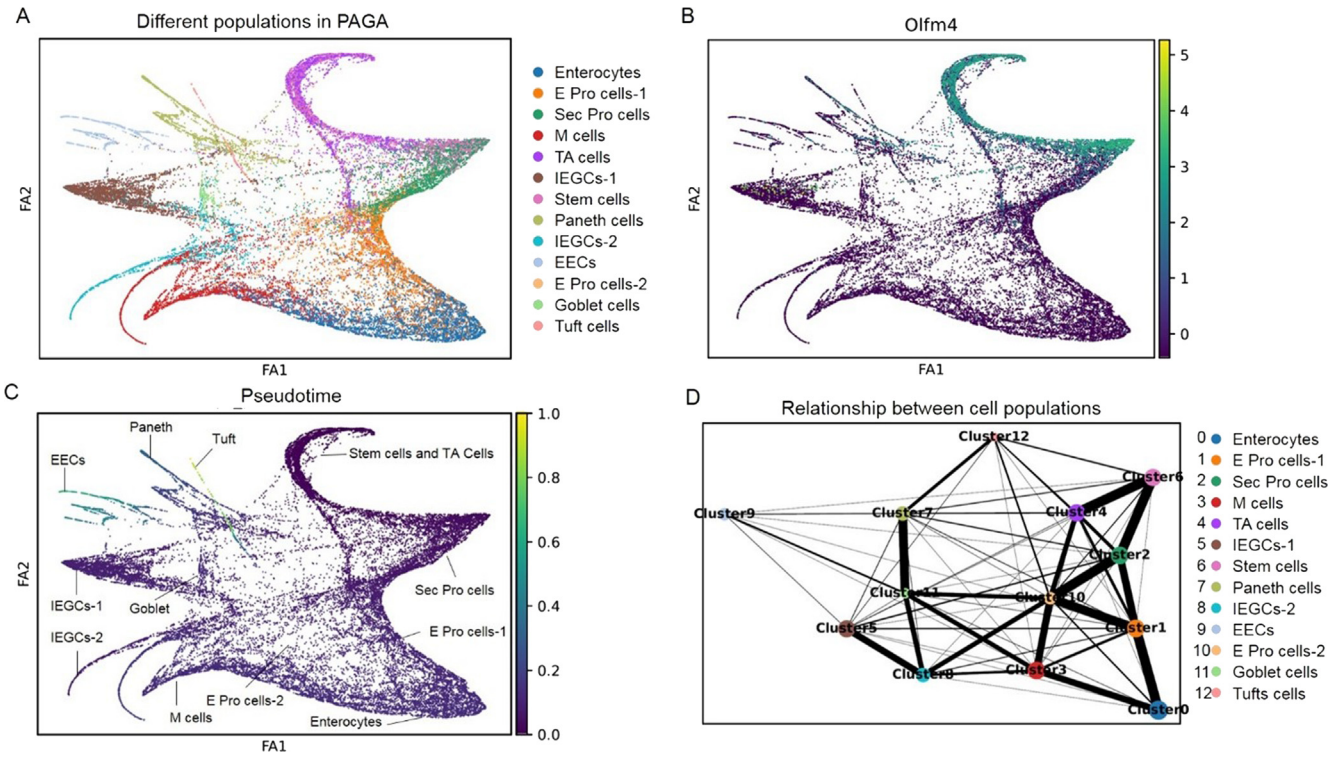

Supplementary Figure 6. The pseudotime of the appearance of each population and the relationship between cell populations analyzed via PAGA. (*A*) PAGA manifold map of the 13 cell populations. Sec, secretory; Pro, progenitor; E, enterocyte. (*B*) The same map with the expression levels of the stem cell marker gene, Olfm4. (*C*) The same map with pseudotime indicated by color. The manifold connections and the relative order of pseudotime suggest a progression from stem cells and TA cells to Sec/E Pro cells and IEGCs to the fully differentiated cell populations in the order of enterocytes, M cells, goblet cells, Paneth cells, EECs, and tuft cells. (*D*) The graph of relationships between various cell types within the manifold. Line thickness indicates the degree of similarity between patterns of gene expression.

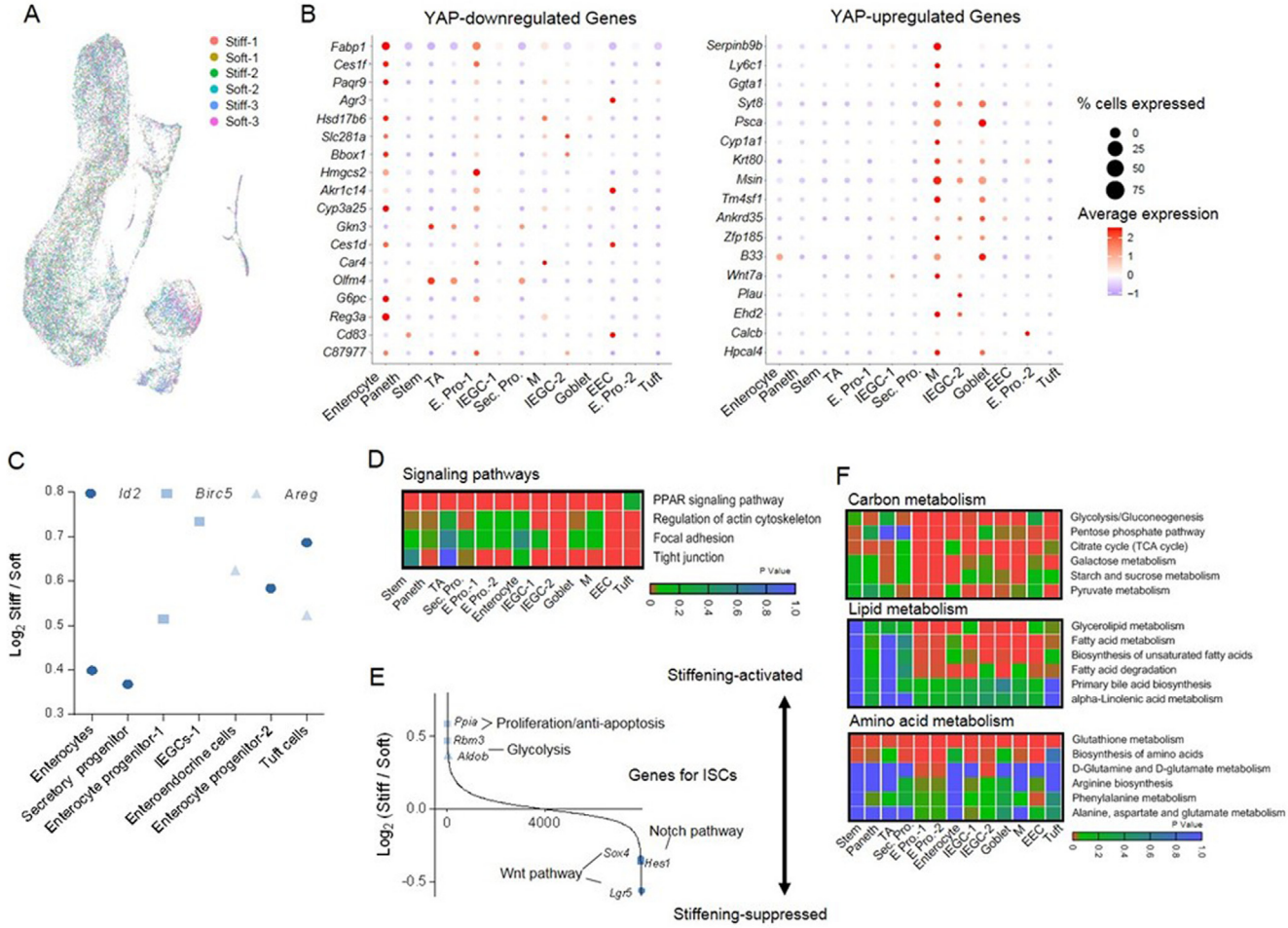

Supplementary Figure 7. (*A*) Three animals were used to triplicate the single-cell expression profiles. The clustering was consistent among the triplications on both the soft matrix and the stiff matrix. (*B*) Genes down-regulated by YAP were highly expressed in enterocytes and their progenitors-1, and genes up-regulated by YAP were highly expressed in goblet cells, IEGCs, and M cells (n = 3). (*C*) Differential gene expressions analysis shows the changes in downstream genes of nuc-YAP (n = 3). (*D*) Pathway enrichment analysis showed that mechanotransduction-related signaling as well as Peroxisome proliferator-activated receptor were more enriched on the stiff matrix. (*E*) Differential gene expression analysis for the ISC population demonstrated that stiffening suppressed both WNT signaling (eg, *Lgr5* and *Sox4* genes) and NOTCH signaling (eg, *Hes1*), in addition to increasing glycolysis (eg, *Aldob* gene) and proliferation (eg, *Ppia* and *Rbm3* genes). (*F*) Pathway enrichment analysis was performed for carbon metabolism, lipid metabolism, and amino acid metabolism. Compared with the soft matrix, carbon metabolism was more enriched than amino acid metabolism on the stiff matrix.

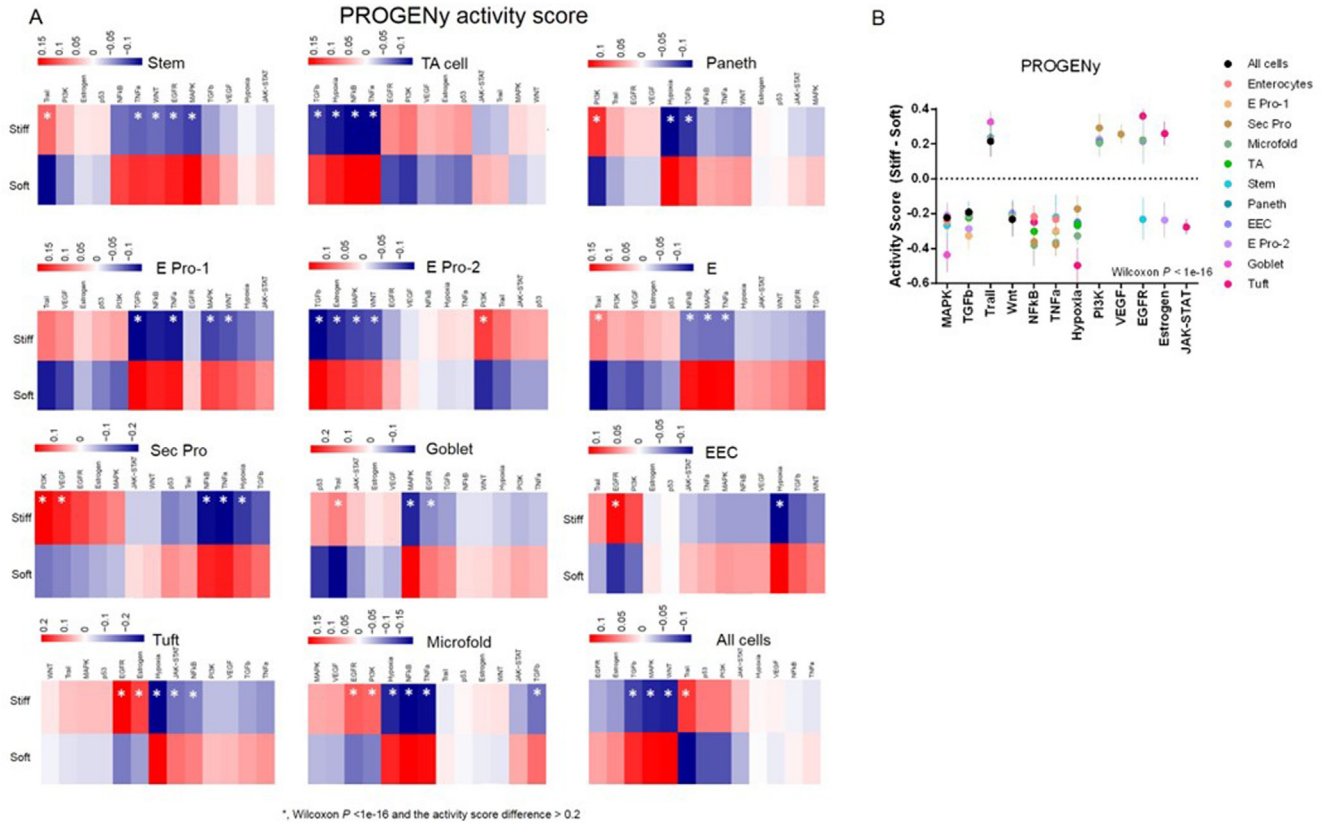

Supplementary Figure 8. (*A*) The PROGENy activity scores of each cell population and all the cells on soft vs stiff substrates. *P* value were calculated using 2-sided Wilcoxon test. If $P < 1e\text{-}16$ and the activity score difference between the soft and stiff substrates was >0.2, the pathway activation was considered significantly different. (*B*) The activity score differences of the significant pathways. For all the cells, WNT, TGF-β, and MAPK pathways were more activated on the soft substrate, and TRAIL pathways were more activated on the stiff substrate. ISCs and enterocyte progenitor cells contributed to the different WNT activity on soft vs stiff substrates; Microfold cells and enterocyte progenitor cells to the TGF-β activity; and ISCs, enterocyte progenitor cells, and goblet cells to the activities of TRAIL and MAPK pathways. In addition, stiff substrate suppressed the nuclear factor kappa-light-chain-enhancer of activated B cells (NF-κB) pathway activity of enterocytes and their progenitors, TA cells, secretory progenitor cells, Microfold cells, and Tuft cells; the tumor necrosis factor alpha (TNF-α) pathway activity of ISCs, enterocytes and their progenitors, secretory progenitor cells, and Microfold cells; the Hypoxia pathway activity of ISCs, TA cells, secretory progenitor cells, Microfold cells, EECs, and Tufts cells; the EGFR pathway activity of ISCs; the estrogen pathway activity of enterocyte progenitor cells; and the JAK-STAT pathway activity of tuft cells. Conversely, the stiff substrate activated the PI3K pathway of secretory progenitor cells, enterocyte progenitor cells, TA cells, and Microfold cells; the VEGF pathway of secretory progenitor cells; the EGFR pathway of Tuft cells, Microfold cells and EECs; and ESTROGEN of tuft cells.

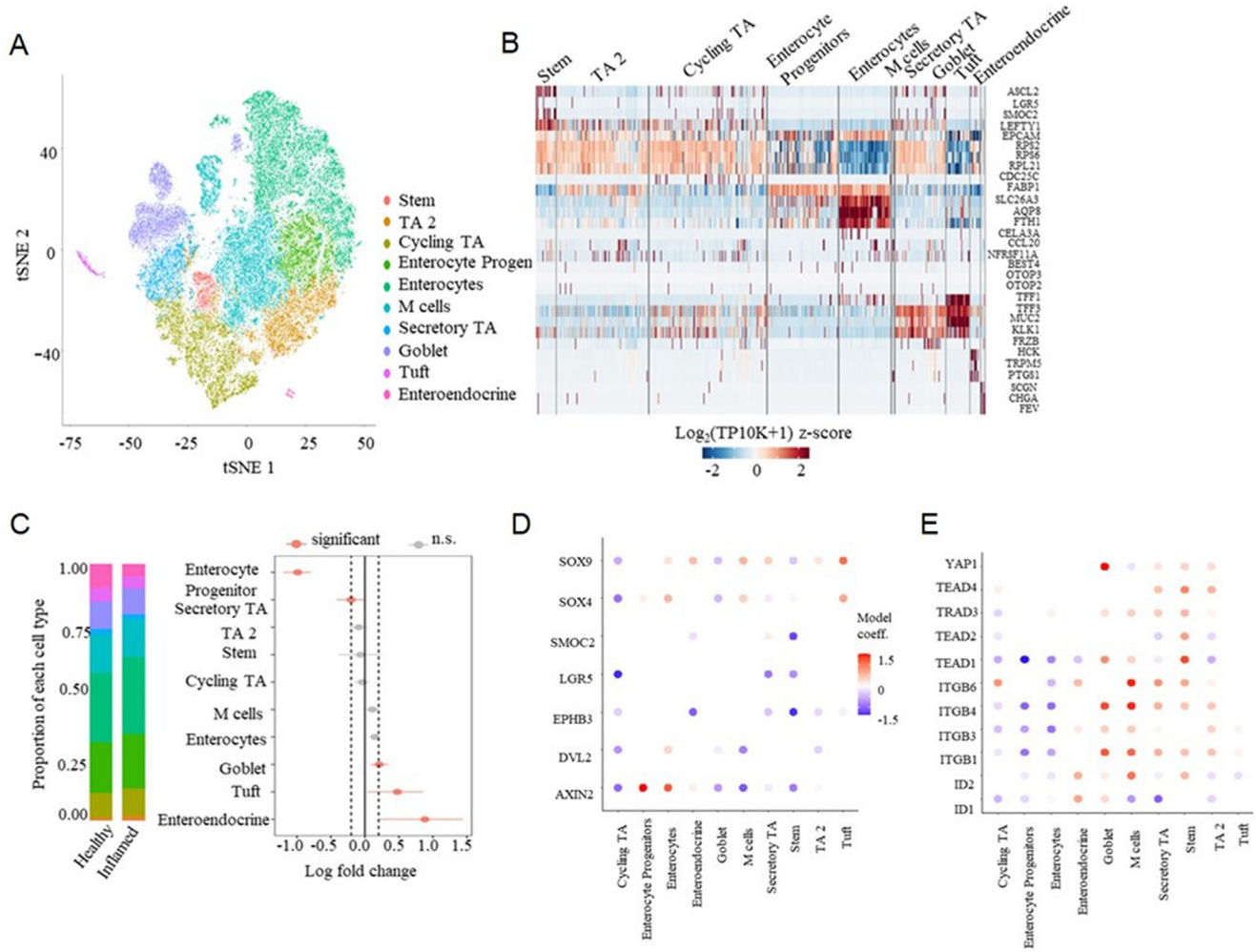

Supplementary Figure 9. ScRNAseq analysis from healthy vs inflamed tissues biopsied from patients with UC (n = 3) and healthy individuals (n = 5), respectively. (*A*) T-Stochastic Neighborhood Embedding of cells colored by cell type from all samples. (*B*) Marker genes for each cell type. (*C*) *Left*: Average proportions of each cell type in aggregates of healthy or inflamed samples. *Right*: Fold changes in the proportion of each cell type in patients with UC compared with healthy individuals. Whiskers correspond to the highest and lowest points within a 1.5 interquartile range. Significant criteria, $P < 0.05$. (*D*) The WNT pathways (eg, *SOX4*, *SOX9*, *LGR5*) suppressed specifically by YAP are down-regulated in the ISCs of UC. The model coefficient reported here is the discrete component of the hurdle model. (*E*) The mechanosignaling pathways, including *INTEGRIN* (*ITGB*), *YAP*, and *TEAD*, are highly activated in both ISCs and the secretive cell types of UC, but not in enterocytes.

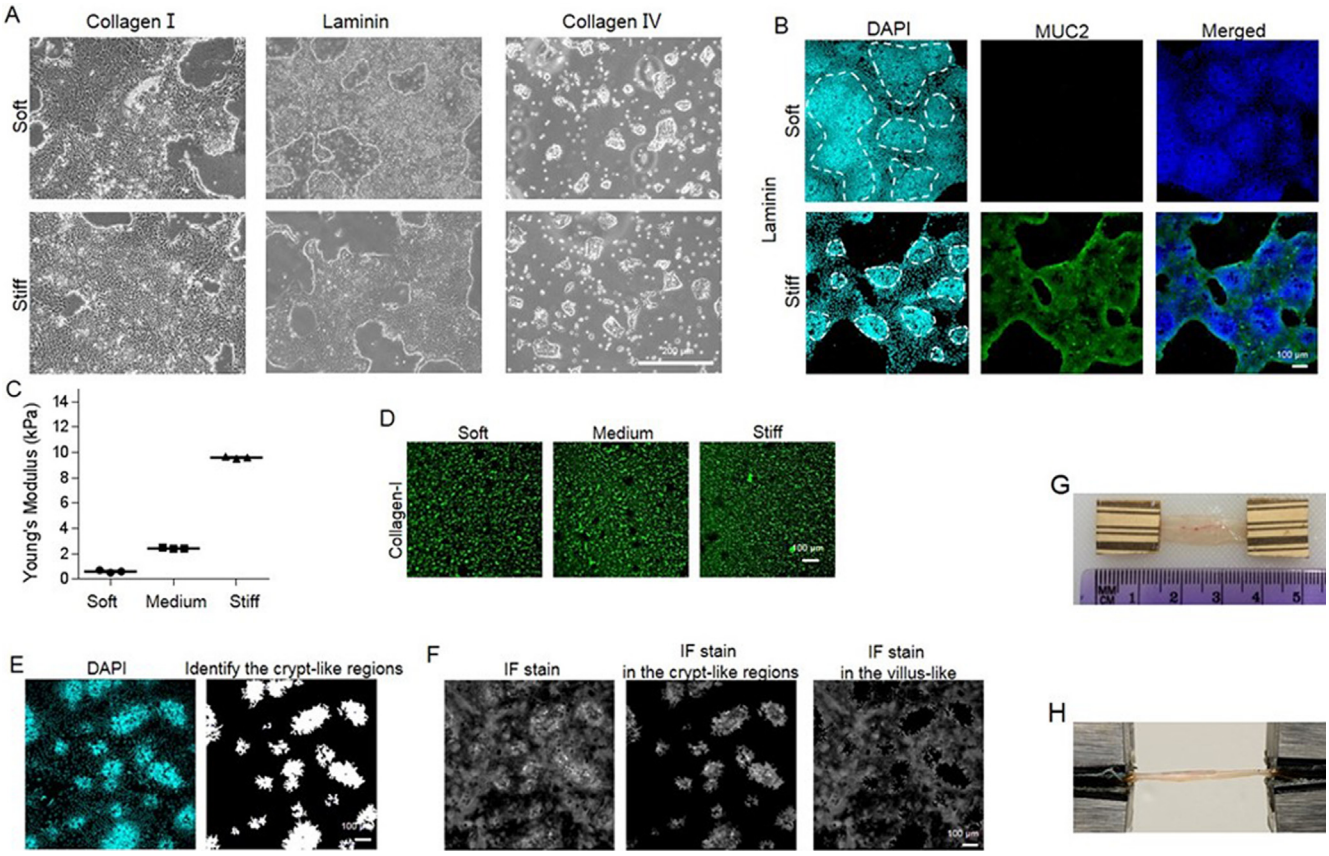

Supplementary Figure 10. (*A*) Phase images on Day 11 after seeding show that Collagen I provided the best support for long-term spreading and growth, with laminin ranking second best. Collagen IV only supported small colonies. Scale bar, 200 μm. (*B*) Increasing the stiffness of the laminin-coated hydrogels diminished crypt size and promoted MUC2^{+} goblet cell differentiation. Scale bar, 100 μm. (*C*) The stiffness of the hydrogel was measured using atomic force microscopy microindentation. The mean values for soft, medium, and stiff gels are 0.6 kPa, 2.4 kPa, and 9.6 kPa, respectively. (*D*) IF staining showed uniform collagen-I coating on the soft, medium, and stiff matrices. Scale bar, 100 μm. (*E*) Illustration of the custom-made MATLAB code. The crypt-like regions were identified based on the intensity of the DAPI staining. Scale bar, 100 μm. (*F*) The fluorescent signals were isolated in the crypt-like regions and the villus-like regions, respectively. Scale bar, 100 μm. (*G*) An intestinal tissue sample with sandpaper tabs at both ends; and (*H*) uniaxial tensile test of the intestinal tissue sample.

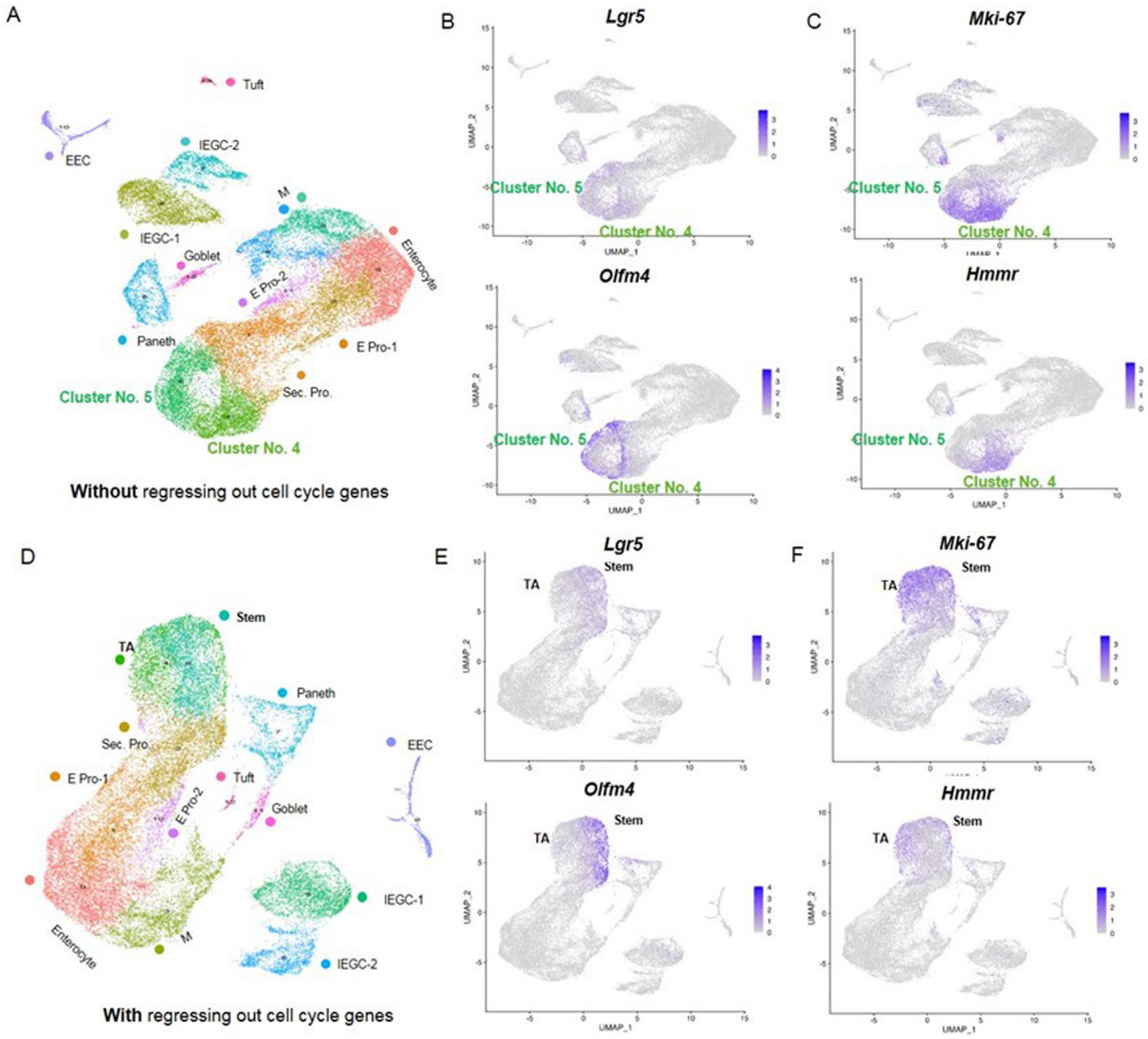

Supplementary Figure 11. Justification for the regression of cell cycle genes in the analysis of scRNAseq. (*A*) Cell clusters were identified based on marker genes without regressing out cell cycle gene expression. When the cell cycle genes are included in the clustering, the expression of the stem cell marker genes (such as *Lgr5* and *Olfm4*) were uniformly expressed in both Clusters 4 and 5 (*B*), while the cell cycle genes (such as *Mki67* and *Hmmr*) were primarily expressed in only Cluster 4 (*C*). (*D*) Cell clusters were identified after regressing out cell cycle gene expression. Two distinct clusters could be identified for the ISCs (*E*) and TA cells (*F*) based on the higher expression of stem cell markers in ISCs than in TA cells.

Supplementary Table 1. Human Sample Information

Sample ID	Patient ID	Gender	Disease	Location
1	U1	Male	UC	Left_colon
2	U1	Male	UC	Transverse_colon
3	U1	Male	UC	Sigmoid_colon
4	U2	Male	UC	Transverse_colon
5	U2	Male	UC	Sigmoid_colon
6	U3	Male	UC	Right_colon
7	U3	Male	UC	Transverse_colon
8	U3	Male	UC	Sigmoid_colon
9	C1	Male	CD	Ileum
10	C2	Male	CD	Ileum
11	C3	Male	CD	Ileum

ID, identification.